Biogeosciences Discuss., 9, 8475–8539, 2012
www.biogeosciences-discuss.net/9/8475/2012/
doi:10.5194/bgd-9-8475-2012

Biogeosciences Discussions

Dissolved inorganic carbon and alkalinity fluxes from coastal marine sediments: model estimates for different shelf environments and sensitivity to global change

V. Krumins[1,*], M. Gehlen[2], S. Arndt[3], P. van Cappellen[4], and P. Regnier[1,5]

[1]Department of Earth Sciences – Geochemistry, Faculty of Geosciences, Utrecht University, 3584CD Utrecht, The Netherlands
[2]LSCE/IPSL, Laboratoire des Sciences du Climat et de l'Environnement, 91191 Gif-sur-Yvette Cedex, France
[3]School of Geographical Sciences, University of Bristol BS8 1SS Bristol, UK
[4]Department of Earth and Environmental Sciences, University of Waterloo, Waterloo, ON N2L 3G1, Canada
[5]Department of Earth and Environmental Sciences, CP 160/02, Université Libre de Bruxelles, 1050 Brussels, Belgium
[*]now at: Department of Environmental Sciences, Rutgers University, New Brunswick, NJ, USA

Received: 30 May 2012 – Accepted: 6 June 2012 – Published: 17 July 2012

Correspondence to: V. Krumins (krumins@envsci.rutgers.edu)

Published by Copernicus Publications on behalf of the European Geosciences Union.

BGD
9, 8475–8539, 2012

Abstract

We present a one-dimensional reactive transport model to estimate benthic fluxes of dissolved inorganic carbon (DIC) and alkalinity (A_T) from coastal marine sediments. The model incorporates the transport processes of sediment accumulation, molecular diffusion, bioturbation and bioirrigation, while the reactions included are the redox pathways of organic carbon oxidation, re-oxidation of reduced nitrogen, iron and sulfur compounds, pore water acid-base equilibria, and dissolution of particulate inorganic carbon (calcite, aragonite, and Mg-calcite). The coastal zone is divided into four environmental units with different particulate inorganic carbon (PIC) and particulate organic carbon (POC) fluxes: reefs, banks and bays, carbonate shelves and non-carbonate shelves. Model results are analyzed separately for each environment and then scaled up to the whole coastal ocean. The model-derived estimate for the present-day global coastal benthic DIC efflux is 126 $\mathrm{Tmol\,yr^{-1}}$, based on a global coastal reactive POC depositional flux of 117 $\mathrm{Tmol\,yr^{-1}}$. The POC decomposition leads to a carbonate dissolution from shallow marine sediments of 7 $\mathrm{Tmol\,yr^{-1}}$ (on the order of 0.1 $\mathrm{Pg\,C\,yr^{-1}}$). Assuming complete re-oxidation of aqueous sulfide released from sediments, the effective net flux of alkalinity to the water column is 29 $\mathrm{Teq\,yr^{-1}}$, primarily from PIC dissolution (46 %) and ammonification (33 %). Because our POC depositional flux falls in the high range of global values given in the literature, the reported DIC and alkalinity fluxes should be viewed as upper-bound estimates. Increasing coastal seawater DIC to what might be expected in year 2100 due to the uptake of anthropogenic CO_2 increases PIC dissolution by 2.3 $\mathrm{Tmol\,yr^{-1}}$ and alkalinity efflux by 4.8 $\mathrm{Teq\,yr^{-1}}$. Our reactive transport modeling approach not only yields global estimates of benthic DIC, alkalinity and nutrient fluxes under variable scenarios of ocean productivity and chemistry, but also provides insights into the underlying processes.

BGD
9, 8475–8539, 2012

1 Introduction

Based on globally averaged carbon box models driven by atmospheric CO_2, globally averaged land-use changes and climate, Andersson et al. (2005) recently estimated that the coastal ocean currently receives ~80 Tmol (inorganic and organic) C yr^{-1} from terrestrial sources, pumps ~20 Tmol C yr^{-1} from the atmosphere and sequesters on the order of 40 Tmol C yr^{-1} in shallow marine sediments. Because the deposition flux of carbon could exceed its burial flux by a factor of two or so (e.g. Andersson et al., 2005), the dissolved inorganic carbon (DIC) recycling flux from both benthic organic matter degradation and carbonate dissolution may be on the order of 40 Tmol C yr^{-1}. These estimates are supported to some extent by observational evidence (e.g. Mackenzie et al., 2005) and clearly highlight the prominent role of shallow sediments in the global coastal ocean carbon budget. A number of recent studies have also discussed the potential importance of alkalinity (Alk) generation in shallow sediments to the global ocean Alk budget, suggesting that the benthic Alk source could act as negative feedback to rising atmospheric CO_2 conditions and ocean acidification (Chen, 2002; Chen et al. 2003; Thomas et al. 2009; Hu and Cai, 2011). This benthic source of alkalinity to the overlying water column has mainly been attributed to anaerobic degradation pathways of deposited organic matter. For instance, Thomas et al. (2009) propose that the 0.073 Teq yr^{-1} of alkalinity generated in the Wadden Sea are produced by denitrification and sulfate reduction. This release could balance 20–25 % of the CO_2 uptake of the entire North Sea. By extrapolating budgets for the East China Sea, Chen (2002) estimates that continental margin sediments contribute 16–31 Teq yr^{-1} of alkalinity globally, a value which is comparable to the global bicarbonate alkalinity delivered by rivers (Suchet et al., 2003). Hu and Cai (2011), however, obtained a much smaller benthic alkalinity flux of 4–5 Teq yr^{-1} based on whole-ocean estimates of denitrification and sulfate reduction in sediments deposited on the continental shelves.

Because of the limited availability of comprehensive observational data sets that can resolve the heterogeneity of the global coastal ocean, it is nonetheless important to

BGD
9, 8475–8539, 2012

recognize that the quantitative global significance of coastal sediments to the carbon cycle, DIC and Alk generation fluxes remains poorly known. For instance, only a few estimates of PIC deposition fluxes in the coastal zone are available (23–24.5 Tmol yr^{-1}, Table 1), while global estimates of POC deposition fluxes for seafloor depths between 0 and 200 m vary by an order of magnitude (16–183 Tmol C yr^{-1}, Table 1). The large uncertainties associated with the deposition fluxes and post-depositional fate of POC and PIC lead to poorly constrained inorganic carbon budgets and benthic fluxes for shallow marine sediments (see, for example, Schneider et al., 2006).

Most commonly, benthic alkalinity fluxes are derived indirectly by balancing water column budgets, that is, they are not based on an explicit representation of the benthic compartment and the alkalinity-generating early diagenetic processes. However, over the past 3 decades, early diagenetic modeling has greatly improved our mechanistic and quantitative understanding of biogeochemical cycling in marine sediments and should thus be considered a method of choice to quantify benthic Alk and DIC fluxes. A few studies have fully addressed the dynamic interplay between redox processes, driven by organic matter decomposition, and inorganic carbonate dissolution and precipitation (Boudreau and Canfield, 1993; Jourabchi et al., 2005; Burdige et al., 2010). Most early diagenetic modeling studies that explore biogeochemical dynamics in shallow water environments tend nevertheless to be site-specific, with little attempt to extrapolate the results to larger scales. (e.g. Blair and Aller, 1995; Martens et al., 1998; Epping et al., 2002; Berg et al., 2003; Luff and Moll, 2004; Rojas and Silva, 2005; Thullner et al., 2005; Morse and Eldridge, 2007; Dale et al., 2008, 2009; Anggara Kasih et al., 2008; Mogollon et al., 2009). The recent study by Thullner et al. (2009), which quantifies organic carbon oxidation pathways and associated dissolved inorganic carbon (DIC) fluxes along an ocean hypsometry from 100 to 5000 m, is a first step in applying early diagenetic modeling at the global scale. A number of coupled global biogeochemical models such as GENIE (Ridgwell, 2007; Ridgwell and Hargreaves, 2007), CLIMBER and UVic (Archer et al., 2009), and HAMMOC (Palastanga et al., 2011) also apply simplified models of early diagenesis (e.g. muds, Archer et al.,

BGD
9, 8475–8539, 2012

2002, or the DCESS sediment module of Shaffer et al., 2008). However, these global models cannot resolve the shallow ocean dynamics and their diagenetic components are typically based on simplifying assumptions such as considering a single PIC phase (calcite) or neglecting Fe cycling/burial.

The limited quantitative understanding of benthic alkalinity and DIC fluxes from shallow marine environments contrasts with the potential significance of coastal sediments for the global carbon cycle and climate. In particular, our ability to better constrain global coastal ocean C budgets will strongly depend on a better quantification of biogeochemical transformations and fluxes in these shallow sediments. In addition, such quantification will also improve our ability to predict the response of the seafloor to perturbations of the carbon cycle, including productivity changes and acidification of coastal waters. For instance, Andersson et al. (2005) predict that increasing coastal productivity over the next century will significantly alter the CO_2 pumping efficiency of the global coastal ocean. This eutrophication will increase POC deposition fluxes and, because organic carbon metabolism is the major driving force for PIC dissolution in shallow environments (Morse and Mackenzie, 1990), benthic carbonate dissolution will increase. In contrast, model simulations by Andersson et al. (2005) indicate that ocean acidification, and the resulting pH drop of circa 0.3 units predicted by the end of the century (e.g. Caldeira and Wickett, 2003), should have a limited impact on benthic $CaCO_3$ dissolution. Nevertheless, this conclusion requires further investigation because it is drawn from simple mass balance calculations, which do not resolve the complex interplay between the large number of benthic processes.

The purpose of this contribution is to determine the quantitative significance of major early diagenetic processes for the production and consumption of DIC and Alk, as well as their benthic fluxes in coastal ocean sediments, for both present day conditions and in response to coastal ocean eutrophication and acidification scenarios. To this end, a one-dimensional (1-D) reactive transport model (RTM) of benthic organic carbon and inorganic carbon dynamics is presented. We simulate organic carbon oxidation pathways, re-oxidation of reduced nitrogen, iron and sulfur compounds,

BGD
9, 8475–8539, 2012

pore water acid-base equilibria, and dissolution of particulate inorganic carbon (calcite, aragonite, and Mg-calcite). In addition, we distinguish between four different carbonate environments and a number of distinct environmental sub-units that are characterized by different biogeochemical drivers. The RTM is then applied to quantify the impact of early diagenetic reactions on the dissolution of three carbonate phases (calcite, aragonite, and a 15 % Mg-calcite) and the benthic DIC and alkalinity fluxes for each of the identified carbonate environments. We also provide a first-order estimate of the global alkalinity and DIC fluxes from marine sediments to the shallow coastal zone by extrapolating our regional results to the scale of the global coastal ocean. Furthermore, we assess the sensitivity of benthic DIC and Alk fluxes in each environment to uncertainties associated with the benthic iron and sulfur cycles. Finally, we explore the response of DIC and Alk fluxes to changes in organic and inorganic carbon deposition fluxes due to eutrophication and ocean acidification, respectively.

2 Methods

2.1 Model environments

The coastal ocean is one of the most complex and heterogeneous aquatic environments in the Earth system. One way to deal with this heterogeneity is to propose a classification of the coastal ocean into different environments with broadly similar characteristics, organized according to series of hierarchical related system levels (Table 2). Each hierarchical level describes a level of organization that controls DIC and alkalinity fluxes at a specific spatial scale. Processes at higher levels have a direct influence on lower level characteristics and smaller-scales are nested within larger scales.

At the highest hierarchical level (Level I), the coastal ocean can be divided into distinct environments, each characterized by a distinct mode of carbonate production and accumulation (input control). Here, we follow the well-established classification proposed by Milliman and Droxler (1996) into four different types of shallow-water

BGD
9, 8475–8539, 2012

carbonate environments: reefs, banks and bays, "carbonate" shelves, and "non-carbonate" shelves. Reefs comprise coral reefs and lagoons and are the most productive carbonate environments in the present-day ocean. Accumulated carbonates mainly originate from corals and algae and, locally, also from foraminifera (e.g. Milliman, 1993). Banks and embayments encompass tropical and sub-tropical, littoral and sub-littoral environments that are characterized by high rates of carbonate production and accumulation, sustained by benthic algae, molluscs, benthic foraminifera and locally also bryozoans and serpulids (e.g. Stockman et al., 1967; Boscence et al., 1985). In contrast to the reef and bank environments, the production and accumulation of carbonates on continental shelves have certainly not been surveyed to the same extent. Nevertheless, the existing data reveals a bi-modal distribution of carbonate contents in shelf sediments. At Level I, the continental shelf is thus divided according to its carbonate content into carbonate and non-carbonate shelves. In these environments, carbonate production is generally supported by benthic and pelagic production, as well as relict components, such as oysters, ooids and in-situ dead coral reefs (e.g. Milliman, 1993 and references therein).

At the next hierarchical level (Level II), the environmental units identified above should be further subdivided into regions that are characterized by similar controls on carbonate dissolution. Previous research has shown that organic matter degradation exerts a dominant control on benthic carbonate dissolution through the production of metabolic carbon dioxide, the associated lowering of the porewater pH and, thus, the saturation state (e.g. Jahnke et al., 1994). In this context, the magnitude and quality of the organic matter deposition flux is a fundamental control factor of the carbonate dissolution fluxes. In addition, anoxic degradation pathways generally produce alkalinity and, therefore, favour carbonate preservation or even precipitation. Thus, the bottom water concentrations of the dominant terminal electron acceptors O_2, NO_3 and SO_4 are additional control factors on carbonate dissolution, since they determine the relative contribution of aerobic and anaerobic decomposition pathways. However, the spatial variability in the magnitude and quality of the organic matter deposition flux remains

BGD
9, 8475–8539, 2012

extremely difficult to assess, since coastal fluxes generally represent a dynamic mixture of organic matter from terrestrial, lateral and in situ sources (e.g. Mollenhauer and Eglinton, 2007; Mollenhauer et al., 2005). This lack of quantitative understanding about the fate of coastal organic matter is also reflected in the large variability in the global estimates of organic matter deposition fluxes for seafloor depths between 0 and 200 m (16–183 Tmol C yr^{-1}, Table 1) and in model-derived degradation rate constants (Arndt et al., 2011).

Therefore, further regionalization based on organic matter and redox criteria is not achievable at this stage and we choose to extract average environmental conditions for each of the four environmental units selected at Level I, only. Values are either extracted from the literature or derived from the 1° dataset of the Levitus94 database (NOAA World Ocean Atlas 1994, available online at http://iridl.ldeo.columbia.edu/). This simplified approach can be seen as a first step towards a better regional classification of the coastal ocean in terms of the dominant controls on carbonate chemistry. It also implies that our results only provide a first-order global estimate of DIC and alkalinity fluxes for the coastal ocean.

On a local scale, depositional fluxes, bottom water concentrations and transport parameters often show a strong correlation with water depth (e.g. Soetaert et al., 2002; Epping et al., 2002). Pressure and, thus, water depth also directly affects the solubility products of the various carbonate phases. Water depth is thus used at Level III of our classification and we assume an average value of 25 m for the reefs, and the banks and bays. The shelves are further subdivided into three depth ranges: 0–50 m, 50–100 m, and 100–200 m. These depths intervals contribute 41, 31, and 28 % of the global coastal seafloor area shallower than 200 m, respectively, based on the data of Smith and Sandwell (1997) extracted from a $\sim 1/2$ min regridding from 72° N to 72° S, accessed online at http://www.grdl.noaa.gov/cgi-bin/bathy/bathD.pl.

BGD
9, 8475–8539, 2012

2.2 Model approach

A 1-D reactive transport model for coastal sediments is developed using the Biogeochemical Reaction Network Simulator (Regnier et al., 2002; Aguilera et al. 2005), which has previously been used to simulate mixed kinetic-equilibrium reaction networks describing early diagenesis (e.g. Jourabchi et al., 2005; Thullner et al., 2005). The vertical concentration fields in the sediment are modeled using the 1-D advection-diffusion-reaction equations:

$$\frac{\partial(\varphi C_i)}{\partial t} = \frac{-\partial(\omega\varphi C_i)}{\partial x} + \frac{\partial}{\partial x}\left\{(D_\mathrm{b} + D_i)\frac{\partial(\varphi C_i)}{\partial x}\right\} + \alpha_i(C_{i_0} - C_i) + \sum R_i \quad (1)$$

and

$$\frac{\partial((1-\varphi)C_i)}{\partial t} = \frac{-\partial(\omega(1-\varphi)C_i)}{\partial x} + \frac{\partial}{\partial x}\left\{D_\mathrm{b}\frac{\partial((1-\varphi)C_i)}{\partial x}\right\} + \sum R_i \quad (2)$$

for solutes and solid-bound species, respectively. In the above equations, x is depth below the sediment-water interface (cm), and φ = porosity [ ], ω = linear sediment burial rate [cm$\dot{\mathrm{y}}\mathrm{r}^{-1}$], C_i = concentration of species i at depth x and time t [$\mu\mathrm{mol\,cm}^{-3}$], C_{i_0} = concentration of i at sediment-water interface [$\mu\mathrm{mol\,cm}^{-3}$], D_b = bioturbation coefficient [$\mathrm{cm}^2\,\mathrm{yr}^{-1}$], D_i = molecular diffusion coefficient of solute species i [$\mathrm{cm}^2\,\mathrm{yr}^{-1}$], α_i = non-local bioirrigation coefficient [yr^{-1}], and ΣR_i = net rate of all reactions involving species i [$\mu\mathrm{mol\,cm}^{-3}\,\mathrm{yr}^{-1}$].

A discretized version of Eq. (1) is solved with an operator splitting approach for the transport and reaction terms. Solute transport is discretized using the Crank-Nicholson algorithm, while for solids and sorbed species (Eq. 2) a flux limiting total variation diminishing scheme is used (e.g. Regnier et al., 1998). The reaction term is cast as a set of Differential Algebraic Equations (DAEs) and solved using a Newton algorithm (for further details, see Aguilera et al., 2005; Centler et al., 2010). A 5×10^{-6} yr time step is imposed for transient simulations that are run until steady state (generally reached

BGD
9, 8475–8539, 2012

after 200–400 simulation years). The modeled sediment thickness is 50 cm, discretized in 116 irregularly spaced nodes.

2.3 Transport

The choice of transport parameters is guided by empirically determined global values or global relationships proposed in the literature. The sediment advection (burial) rate (ω) and bioturbation coefficient (D_{b_0}) are obtained from the global depth relationships proposed by Middelburg et al. (1997):

$$\omega = 3.3 \times 10^{(-0.87478367 - 0.00043512 \cdot \mathrm{SFD})} \quad (3)$$

$$D_{b_0} = 5.2 \times 10^{(0.76241122 - 0.00039724 \cdot \mathrm{SFD})} \quad (4)$$

where SFD is the seafloor depth in m.

A global average bioturbation depth of 10 cm in marine sediments (Boudreau, 1994) is assumed for all environments and water depths. An exponential decay function is imposed for the porosity (φ) depth profile (Wang and van Cappellen, 1996):

$$\varphi(x) = 0.75 + 0.1e^{-0.15x}. \quad (5)$$

Diffusion coefficients for the dissolved species are corrected for temperature and sediment porosity according to Boudreau (1996). Bioirrigation intensity is assumed to decrease exponentially with depth in the sediment:

$$\alpha(x) = \alpha_0 \cdot e^{(-x/x_{\mathrm{irr}})} \quad (6)$$

where α_0 is the bioirrigation coefficient at the sediment-water interface (yr^{-1}), and x_{irr} is a depth attenuation coefficient (cm). The value of x_{irr} is set to 3.5 cm, while α_0 is estimated following Thullner et al. (2009).

Some of the dissolved oxygen that is transported into the sediment via bioirrigation will oxidize reduced iron in the vicinity of burrows. The iron (oxy)hydroxide precipitates

BGD
9, 8475–8539, 2012

sorb aqueous phosphate (e.g. Spiteri et al., 2008), hence reducing the apparent irrigational transport of phosphate. Berg et al. (2003) and Meile et al. (2005) showed that effective bioirrigation rates differ widely among chemical species depending on their behavior at burrow walls. For instance, according to Berg et al. (2003), $\alpha \approx 0$ for Fe^{2+}. Rather than modifying α (in Eq. 1), Katsev et al. (2007) reduced the local concentrations of Fe^{2+} and phosphate by a factor of 0.1 to account for reduced bio-irrigation. Here, we chose to multiply α calculated according to Eq. (6) by 0.01 for Fe^{2+} and $H_2PO_4^-$. This corresponds roughly to the ratio of the depth integrated α value for Fe^{2+} to that of solutes such as O_2 or NH_4^+ in Meile et al. (2005).

2.4 Reactions

2.4.1 POC hydrolysis (R1–2)

Organic matter in the sediments is assumed to have Redfield stoichiometry: $(CH_2O)_{106}(NH_3)_{16}(H_3PO_4)$ (Table 3, R1 and R2). Organic matter degradation is modeled as a two-step process. It is first hydrolyzed to yield dissolved organic carbon (DOC), ammonia and phosphate. Hydrolysis rates are assumed to exhibit a first order dependence on the concentrations of the reactive POC pools. Ammonia released during POC hydrolysis is protonated to ammonium (NH_4^+), while phosphate is released as dihydrogen phosphate ($H_2PO_4^-$), the predominant form under typical pore water pH conditions. The hydrolysis products (represented as DOC) are treated as reactive intermediates, which are oxidized via one of the primary redox pathways (Sect. 2.3.2). The input of POC to the sediment is assumed to consist of two reactive pools and one refractory pool: 80 % of the reactive organic carbon flux (67 % of the total organic carbon flux globally) is allocated to the highly reactive POC pool, which is hydrolyzed with a rate constant of $1\,yr^{-1}$, while the other 20 % of the reactive organic carbon flux (17 % of the total organic carbon flux) is more slowly hydrolyzed, with $k = 0.1\,yr^{-1}$. The reactivity, k_1, of the most reactive POC fraction is representative for phytoplankton derived POC and falls within the typical range of 10^0–$10^1\,yr^{-1}$ reported in the literature

BGD
9, 8475–8539, 2012

(e.g. Westrich and Berner, 1984; Henrichs and Doyle, 1986; Burdige, 1991). Aged or re-suspended organic matter is usually less reactive and typical values reported in the literature range between 10^{-1}–10^{0} yr^{-1} (e.g. Westrich and Berner 1984). The third POC pool of refractory organic matter represents 16 % of the total carbon pool and is assumed to be unreactive, $k = 0.0\,yr^{-1}$ on the timescales considered here. It is not explicitly modeled, but it is included in sulfidization reactions and in C budget estimates.

2.4.2 Primary redox reactions (R3–6)

The primary redox reactions of aerobic oxidation, denitrification, iron reduction, and sulfate reduction are coupled to DOC oxidation (Table 3). For the depositional conditions considered, sulfate is never entirely exhausted when reaching the bottom of the early diagenetic zone ($x = 50\,cm$); hence, methanogenesis is assumed to be of minor importance in organic matter degradation. This is consistent with observations and model results for shelf sediments receiving high organic matter inputs which show that the depth scale for the onset of methanogenesis is typically on the order of a couple of meters or more (e.g. Dale et al., 2008; Regnier et al., 2011). The rates of the primary redox reactions are assumed to exhibit a first-order dependence on the concentration of DOC and a Michaelis-Menten-type dependence on the concentration of the terminal electron acceptor (Table 4). In addition, the rates of the different electron accepting pathways are scaled by their relative yields (Table 4). Yield values and half-saturation constants are taken from Thullner et al. (2005) (Table 5). The anaerobic processes are also non-competitively inhibited by oxygen. The inhibition constant for denitrification is set to result in 90 % inhibition when $[O_2] = 63\,\mu M$ ($2\,mg\,l^{-1}$), while those for iron and sulfate reduction lead to 90 % inhibition at $[O_2] = 6\,\mu M$ ($0.2\,mg\,l^{-1}$). The overall DOC oxidation rate constant k_3 is common to all anaerobic respiration pathways.

BGD
9, 8475–8539, 2012

2.4.3 PIC dissolution (R11–13)

The rates of dissolution of the PIC phases are computed using:

$$R_{\text{dissolution}} = k \cdot (1 - \Omega)^n \cdot C \quad (7)$$

where C is the concentration of the PIC phase and Ω, the saturation state, is given by

$\Omega = [Ca^{2+}] \cdot [CO_3^{2-}]/K_{SP}$ for calcite and aragonite, and

$\Omega = [Ca^{2+}]^{0.85} \cdot [Mg^{2+}]^{0.15} \cdot [CO_3^{2-}]/K_{SP}$ for 15 % Mg-calcite.

The apparent solubility products (K_{SP}) of calcite and aragonite are calculated as a function of temperature, pressure and salinity according to Millero (1995), and the apparent solubility product of 15 % Mg-calcite in seawater is assumed to be 21 % greater than that of aragonite, based on the findings of Morse et al. (2006). The kinetic parameters k and n for calcite, aragonite and 15 % Mg-calcite are obtained from Walter and Morse (1985) using *Balanus*, *Halimeda*, and *Peneroplis* data, respectively. The experimentally-determined rate constants k are multiplied by a factor 0.1 to account for the effects of inhibitors, surface poisoning and coatings that are likely to reduce the dissolution kinetics of PIC in natural sediments.

Pore water calcium concentrations are explicitly computed, while the concentration of pore water magnesium is expected to vary little, and is kept constant at the average seawater value of 53 mM. Although porewaters may be oversaturated with respect to one or more $CaCO_3$ phases, in situ precipitation of non-biogenic $CaCO_3$ in sediments is believed to be of limited importance, relative to dissolution, due to inhibition by organic compounds and magnesium (Morse and Mackenzie, 1990; Morse and Mucci, 1984). As a result, non-biogenic carbonate precipitation is not included in the reaction network.

2.4.4 Other reactions

Dissociation of H_2O, H_3BO_3, H_2S, H_2CO_3 and HCO_3^- are modeled as equilibrium reactions. The apparent equilibrium constants are adjusted for salinity, temperature and

BGD
9, 8475–8539, 2012

pressure according to Millero (1995). Secondary redox reactions; that is, reoxidation reactions of reduced by-products of organic matter degradation are also considered. The reactions included are the oxidation of ammonia, hydrogen sulfide, iron sulfides and ferrous iron by oxygen (R7–10). Iron sulfide precipitation and its conversion to pyrite are included in the reaction network, as is iron carbonate precipitation (R14–16).

Soluble ferrous iron, ammonium, and phosphate are assumed to adsorb non-specifically to solids. Specific phosphate sorption onto ferric iron phases is also modeled. The sorbed-P, sorbed-NH_4^+, sorbed-Fe(II) and iron(III)-sorbed-P are treated as solid-bound constituents in equilibrium with the pore water phase. Finally, refractory organic matter, which is not otherwise modeled, is assumed to react with sulfide during the process of sulfurization (R17).

2.5 Boundary conditions

2.5.1 Baseline scenario

The published estimates of global carbon (POC and PIC) deposition and burial fluxes are summarized in Table 1. In the absence of a robust regionalization of POC fluxes for the global coastal ocean, the degradable POC flux for the carbonate shelves, non-carbonate shelves, and banks and bays are estimated using the depth relationship for the benthic oxygen consumption of coastal sediments by Soetaert et al. (2002):

$$J_{POC} = 40.61 \cdot SFD^{-0.571} \quad (8)$$

where J_{POC} is the degradable POC flux in mol C m^{-2} yr^{-1}. Thus, the reactive POC deposition fluxes for the 25 m, 75 m, and 150 m shelf depths are 6.5, 3.5, and 2.3 mol m^{-2} yr^{-1}, respectively (Table 6a) For the "banks and bays" environment, the reactive POC flux calculated from Eq. (8) assuming 25 m SFD (= 6.5 mol m^{-2} yr^{-1}) is also used. The imposed reactive POC deposition flux for reefs, 5.2 mol C m^{-2} yr^{-1}, corresponds to the estimated average net primary productivity of coral reef ecosystems (Hatcher, 1990). When integrated over the total surface area of the coastal ocean

BGD
9, 8475–8539, 2012

(SFD ≤ 200 m), the resulting global reactive POC flux estimate is 117 Tmol yr^{-1}. This value falls within the range of published values for global coastal POC deposition flux (16 to 183 Tmol yr^{-1}), but is somewhat higher than the average value (94 Tmol yr^{-1}) of all the studies reported in Table 1, including the ~60 Tmol yr^{-1} estimate of Mackenzie et al. (2005). In addition, estimates of the average global POC burial in coastal sediments (Table 1) indicates that global coastal sediments receive an additional 22.4 Tmol yr^{-1} of POC that is refractory on the considered time scale. The total global coastal POC deposition flux thus amounts to 140 Tmol yr^{-1}. A major source of uncertainty for the DIC and alkalinity fluxes is the very limited number of studies that provide estimates of global coastal PIC deposition fluxes (Table 1). The PIC deposition fluxes are taken from Milliman and Droxler (1996), and range from 0.27 mol m^{-2} yr^{-1} for "non-carbonate" shelves to 15 mol m^{-2} yr^{-1} for coral reefs. Published estimates for the global average fraction of aragonite in marine PIC rain range from 10 % to 50 %, and may be as high as 75 % (Munhoven, 2007). On the shelves, we divide the PIC deposition flux into 35 % aragonite and 65 % calcite, based on the estimates of pelagic PIC production by Gangstø et al. (2008). For the reefs and banks and bays, PIC is divided into aragonite, calcite and Mg-calcite in the ratios 63:13:24 (Land, 1967). The PIC flux in a given coastal environment is assumed to be independent of SFD (Table 6a). We expect that, while benthic productivity will decrease with increasing seafloor depth, planktonic production may actually increase because of increased habitat volume. Furthermore, the Koeve (2002) relationship of the POC:PIC ratio with depth in the Atlantic basin (POC:PIC = $64.3 \cdot \mathrm{SFD}^{-0.56}$), when combined with the Soetaert POC deposition flux relationship (Eq. 8), results in a nearly depth-independent relationship for the PIC flux (= $0.63 \cdot \mathrm{SFD}^{-0.011}$ mol m^{-2} yr^{-1}), which is very close to Milliman and Droxler's estimate for PIC deposition on carbonate shelves (0.60 mol m^{-2} yr^{-1}). Note that our globally integrated PIC deposition flux for the coastal zone is also in agreement with the value used by Andersson et al. (2005) (Table 1).

Raiswell (2006) estimated the global delivery of highly reactive iron to the shelves to be 53 Tg yr^{-1}, primarily from rivers, atmospheric dust, and diagenetic recycling.

BGD
9, 8475–8539, 2012

Dividing by the shelf area, this gives an average deposition flux of 0.036 mol Fe m^{-2} yr^{-1}, which we scale with the sediment burial rate in order to estimate the reactive iron deposition in the various environments and water depth ranges (Table 6a).

Bottom water temperature, oxygen concentration, and nitrate concentration are extracted from the 1° dataset of the Levitus94 database. For each latitude and longitude in the dataset, the deepest water depth with data available is taken as representative of bottom water, and the corresponding (temperature, oxygen or nitrate) values are inferred to be the bottom water values. Over the 0–200 m SFD range, no significant relationship exists between bottom water [O_2] and water depth ($p > 0.05$), therefore the average oxygen concentration (0.195 mM) is used. Nitrate and temperature are both water depth dependent (Table 6a). The average bottom water temperature is used along with pressure only to calculate K_{SP} values for aragonite and calcite (Millero, 1995) and the apparent equilibrium constants for the dissociation of weak acids. The global average temperature for coral reefs, 27.6 °C (Kleypas et al., 2005), is used as bottom water value for the reefs.

Analysis of the GLODAP database for stations with seafloor depths ≤200 m (accessed from http://cdiac.ornl.gov/ftp/oceans/GLODAP_bottle_files/) indicates that dissolved inorganic carbon (DIC) also varies with SFD. In contrast, there is no significant correlation between salinity or alkalinity and seafloor depth ($p > 0.05$), so the average values of 34.64 (psu) and 2.306 meq l^{-1} are used. The bottom water alkalinity and DIC concentrations are used to calculate pH and partitioning of the aqueous carbonate species ($H_2CO_3^*/HCO_3^-/CO_3^{2-}$), using the apparent equilibrium dissociation constants adjusted for depth, salinity and temperature (Millero, 1995). Table 6a presents the alkalinity, DIC, pH, [CO_3^{2-}], and aragonite saturation imposed as bottom water boundary conditions.

The total dissolved boron concentration is estimated from salinity according to Millero (1995). The concentrations of SO_4^{2-}, Ca^{2+} and Mg^{2+} at the sediment-water interface are set to 28, 10, and 53 mM, respectively, while bottom water [$H_2PO_4^-$] is assumed to

BGD
9, 8475–8539, 2012

be 0.001 mM. The concentrations of H_2S, HS^-, NH_4^+, Fe^{2+} at the seafloor are assumed to be zero.

2.6 Benthic DIC and alkalinity flux

Because the DIC buried with pore waters is very small (<1 %), and in situ $CaCO_3$ precipitation and $FeCO_3$ precipitation is predicted to be minimal, the benthic DIC efflux is essentially equal to the sum of the depth-integrated rates of POC oxidation and PIC dissolution. For the alkalinity flux the situation is more complicated and can be analyzed as follows.

The alkalinity flux from the sediments, A_{T_out}, can be computed as:

$$A_{T\_out} = Alk_{redox} + Alk_{PICdiss} - Alk_{burial} - 2(FeS, FeS_2, \text{and } FeCO_3, OrgS)_{burial}, \quad (9)$$

where Alk_{redox} and $Alk_{PICdiss}$ represent alkalinity generation by the (primary and secondary) redox reactions and carbonate dissolution, respectively (see Table 3 for individual contributions), Alk_{burial} corresponds to the alkalinity flux associated with porewater burial, and the last term on the right-hand side is the burial flux of reduced Fe^{2+} minerals and organic sulfur (see below). For the baseline simulations, the fraction of generated alkalinity that is buried is small and ranges from 1.3 % at 25 m water depth to 2 % at 150 m water depth.

The effect of removal of FeS by burial on the pore water alkalinity balance can be expressed by writing a net reaction for FeS generation, which combines sulfate and iron reduction (see Carnigan and Tessier, 1988):

$$9CH_2O + 4Fe(OH)_3 + 4SO_4^{2-} + 8H^+ \rightarrow 4FeS + 19H_2O + 9CO_2 \quad (10)$$

BGD
9, 8475–8539, 2012

Similarly, the net effects of burial of FeS_2, $FeCO_3$, and OrgS can be expressed by combining Reactions (R5), (R6), and (R14–R17):

$$17CH_2O + 4Fe(OH)_3 + 8SO_4^{2-} + 16H^+ \rightarrow 4FeS_2 + 17CO_2 + 4H_2 + 27H_2O \quad (11)$$

$$CH_2O + 4Fe(OH)_3 + 3CO_2 \rightarrow 4FeCO_3 + 7H_2O \quad (12)$$

$$2CH_2O + \text{inert-POC} + SO_4^{2-} + 2H^+ \rightarrow 2CO_2 + \text{orgS} + 2H_2O \quad (13)$$

As can be seen from these reaction formulas, burial of reduced iron and sulfur species result in a net production of alkalinity of 4 equivalents per mol FeS_2, 2 equivalents per mol FeS, 2 equivalents per mol organically-bound S(-II), and 0 equivalents per mol $FeCO_3$.

Although the above reactions generate alkalinity, it is important to note that the burial of reduced compounds actually lowers the alkalinity generation compared to that predicted from iron reduction and sulfate reduction alone. For example, in generating one mole of FeS, 2 moles of organic carbon are oxidized via sulfate reduction, and 1/4 via iron reduction (Eq. 10). If we would only consider the primary redox reactions, iron reduction and sulfate reduction would each produce 2 equivalents of alkalinity (1/4 R5 and 2R6), that is, significantly more than the 2 equivalents predicted by Reaction (12). Since the alkalinity generation by the primary redox reactions is already included in Alk_{redox}, for the purpose of alkalinity accounting (in terms of the contribution of individual reactions to the flux through the SWI), the burial of reduced iron species (FeS, FeS_2, and $FeCO_3$) actually decreases alkalinity generation by 2 equivalents per mol Fe^{2+} mineral buried (compared to the predicted alkalinity generation in the absence of Fe^{2+} mineral burial) and this contribution is thus a sink-term in Eq. (9).

A major fraction of the alkalinity efflux A_{T_out} is under the form of reduced solute species (HS^-, H_2S, NH_4^+ and Fe^{2+}), which tend to be short-lived when released in oxygenated waters. Rapid reoxidation of Fe^{2+} near burrow walls and at the water-sediment interface is accounted for by imposing a strongly reduced bioirrigation coefficient (Sect. 2.2). Some of the dissolved iron escaping coastal sediments may be

BGD
9, 8475–8539, 2012

exported laterally to the open ocean, where it may fuel biological productivity (e.g. Dulaiova et al., 2009). In addition, the fate of the benthic ammonium flux in the water column (i.e. nitrification, export, assimilation by phytoplankton as ammonium or nitrate, burial in the sediment) will have an important influence on the coastal ocean alkalinity budget. However, because of the complexity of the problem, a holistic assessment of the influence of the benthic ammonium flux on coastal ocean alkalinity would require a coupled pelagic-benthic model. Our diagenetic model approach can only provide the flux of alkalinity through the sediment-water interface. Based on these considerations, we hypothesize that A_{T_out} calculated with Eq. (9) overestimates the irreversible source of benthic alkalinity to the coastal ocean alkalinity primarily because of the re-oxidation of free sulfide at or near the water-sediment interface, a very rapid reaction (Kaplan et al., 1963; Jørgensen and Fenchel, 1974; Jørgensen, 1978). Because sulfide oxidation exactly cancels the alkalinity generated by sulfate reduction (Table 3), combined sulfate reduction and sulfide oxidation potentially has no effect on water column alkalinity. Although some reduced sulfur can be assimilated, volatilized or exported off-shelf (Chen and Wang, 1999; Chen, 2002; Thomas et al., 2009), it is likely that most of the model-predicted efflux of free sulfide is efficiently oxidized at or near the water-sediment interface. Therefore, we propose that correcting A_{T_out} for the oxidation of H_2S and HS^- provides a more realistic measure for the effective benthic alkalinity flux A_T^* to the coastal ocean:

$$A_T^* = A_{T\_out} - 2 \cdot (HS^- + H_2S)_{out} \quad (14)$$

where the sulfide efflux $(HS^- + H_2S)_{out}$ is calculated directly from the model computed diffusion and bioirrigation fluxes of the two sulfide species. Alternatively, $(HS^- + H_2S)_{out}$ can also be obtained from the sulfide mass balance:

$$(HS^- + H_2S)_{out} = 1/2\ SO_4^{2-}\ \text{reduction} - 1/2\ HS^-\ \text{oxidation} - \text{FeS precipitation} - \text{pyritization} - \text{sulfidization} - (HS^- + H_2S)_{burial} \quad (15)$$

BGD
9, 8475–8539, 2012

where:

$$\text{FeS precipitation} = \text{FeS}_{\text{burial}} + \text{ pyritization } + 1/2\ \text{FeS oxidation} \quad (16)$$

Combining Eqs. (9), (14), (15) and (16), and using the stoichiometries in Table 3, A_T^* can then be expressed as:

$$A_T^* = 8(\text{net Fe reduction}) + 0.14 \cdot \text{ammonification } + 0.8 \cdot \text{denitrification } - \text{ nitrification} + 2(\text{PIC dissolution}) - \text{Alk}_{\text{burial}} + 2(\text{HS}^- + \text{H}_2\text{S} + \text{orgS} - \text{FeCO}_3 + \text{FeS}_2)_{\text{burial}} \quad (17)$$

While Eqs. (14) and (17) are equivalent expressions of A_T^*; the latter equation provides additional insight into the processes that contribute to A_T^*.

2.7 Sensitivity study

Using the 75 m water depth "carbonate" shelf environment as an example, we analyze the sensitivity of benthic DIC and alkalinity production and fluxes to a number of the "internal" model parameters.

2.7.1 Sulfur cycle

The fate of sulfide produced in the process of organoclastic sulfate reduction exerts an important influence on the saturation state of pore waters with respect to carbonates. Sulfide oxidation by oxygen is often the main driver for shallow subsurface carbonate dissolution (Luff and Wallmann, 2003). Yet, published values for sulfide oxidation rate constants range widely. For example, the k_{SulfO_x} value used by Wang and Van Cappellen (1996) is three orders of magnitude greater than the value of Jourabchi et al. (2005), which we use in the baseline scenario. We therefore test k_{SulfO_x} values equal to 10X, 100X, and 1000X the baseline value. In addition, we explore the effect of 0.1X the baseline sulfide bioirrigation coefficient.

BGD
9, 8475–8539, 2012

2.7.2 Iron cycle

Dissimilatory iron reduction generates 8 eq. alkalinity per mol of Fe^{3+} reduced (Table 3), though the effect of iron reduction on sediment alkalinity generation depends on the fate of reduced species, notably Fe^{2+} (see Sect. 2.5). The benthic alkalinity flux will therefore be influenced by the availability of reactive iron in the sediment. However, there is considerable uncertainty in the amount of reactive iron deposition on coastal sediments. While Poulton and Raiswell (2002) estimated that 388 $Tg\,yr^{-1}$ of reactive iron is discharged from rivers globally, we use the more recent estimate of Raiswell (2006) of 58 $Tg\,yr^{-1}$ for the combined inputs from rivers, atmospheric dust, and diagenetic recycling. The resulting average reactive Fe(III) deposition flux is approximately 70 % lower than that used by Thullner et al. (2009) for their 100 m water depth simulations. Here we test the effect of a doubling of the iron (oxy)hydroxide deposition flux on the DIC and alkalinity fluxes in coastal sediments. In addition, simulations are run with 10X the baseline FeS precipitation rate constant.

2.8 Global change scenarios

2.8.1 Global coastal ocean productivity

Over the past decades, human activity has significantly accelerated the supply of land-derived nutrients to the coastal ocean. As a result, nearshore areas experience increase eutrophication with potentially important implications for the global carbon cycling (e.g. Cloern, 2001; Turner and Rabalais, 2003; Mackenzie et al., 2005).

For each environment, we tested a range of reactive POC fluxes from 12.5 % to 150 % of the baseline value, to span the range of published global coastal POC flux values and gain insights into the response of DIC and alkalinity production and fluxes to organic matter fluxes and eutrophication. The sensitivity analysis then focuses on the effects of variations in the POC deposition flux on the partitioning of organic matter

BGD
9, 8475–8539, 2012

degradation between the different oxidation pathways, the fate of PIC, and benthic DIC and A_T fluxes.

2.8.2 Acidification scenario

Ocean acidification is likely to affect biocalcification rates (Andersson et al., 2011) thereby potentially affecting the PIC depositional flux to coastal sediments. Because the non-carbonate shelf boundary conditions are identical to those of the carbonate shelves, except for the 56 % lower PIC deposition flux, we use the baseline non-carbonate shelf model outputs to represent the carbonate shelves under decreased PIC deposition. Decreased PIC deposition in the non-carbonate shelves, reefs, and banks and bays is modeled by imposing a decrease of the PIC deposition flux by 44 % relative to the baseline PIC flux. This decrease in PIC deposition approximately equals the decrease predicted by the year 2100 for the most extreme case considered by Andersson et al. (2005).

The effect of increasing seawater DIC due to increasing atmospheric CO_2 is also tested. Alkalinity and temperature are kept constant and the carbonate system is re-calculated for 2.5 % and 5 % increases in DIC, leading to a drop in bottom water pH of 0.11 and 0.24 pH units, respectively (Table 6b). In all cases, the water column remains oversaturated with respect to the carbonate mineral phases considered.

Although modeling water column carbonate chemistry and ocean-atmosphere CO_2 exchange is beyond the scope of this work, it is useful to estimate the magnitude of the atmospheric CO_2 increase that is needed to produce the imposed changes in the bottom water carbonate system. If the coastal surface water alkalinity, the differences in temperature and DIC between bottom and surface waters, and the surface water undersaturation with respect to atmospheric CO_2 observed in the GLODAP dataset all remain constant, the baseline, +2.5 %, and +5 % bottom water DIC scenarios correspond to 369, 495, and 686 ppm atmospheric CO_2, respectively. These values are close to the atmospheric CO_2 concentrations predicted for the years 2000, 2050, and 2100, respectively, for the IS92a scenario (Joos et al., 1999).

BGD
9, 8475–8539, 2012

3 Results and discussion

3.1 DIC and Alkalinity production and fluxes in the global coastal ocean: baseline scenario

3.1.1 Organic matter degradation: DIC production

The baseline simulations reproduce the typical vertical redox stratification observed in aquatic sediments, with aerobic carbon oxidation occurring nearest the water-sediment interface, followed by denitrification, iron reduction, and sulfate reduction (results not shown). In the early diagenetic scenarios considered here, the degradable POC is consumed within the top 20 cm of sediment, and pore water sulfate never drops below 10 mM. The distribution of organic carbon oxidation over the various primary redox pathways is shown in Fig. 1a, for the baseline scenario simulations. Because for each mole of organic C oxidized one mole of DIC is produced, the figure also shows the contribution of the primary respiration processes to DIC generation.

The total DIC production is determined by the imposed reactive POC deposition fluxes, which range from 6.46 mol C m^{-2} yr^{-1} for the banks and bays and the 25 m water depth shelf environments, to 2.32 mol C m^{-2} yr^{-1} for the 150 m shelf depth. Aerobic respiration accounts for 12 % (25 m water depth shelves, and banks and bays) to 16 % (150 m water depth shelves) of total organic C oxidation, while denitrification and iron reduction account for 2–5 % and 0.3–0.7 % of carbon oxidation, respectively. Sulfate reduction is the main respiratory pathway. For the 25 m water depth shelves and the banks and bays, sulfate reduction explains 85 % of organic C oxidation, while at 150 m water depth, 77 % of C oxidation is coupled to sulfate reduction.

3.1.2 Carbonate dissolution: DIC production

Carbonate mineral dissolution in shallow sediments is driven by POC mineralization and the resulting CO_2 production (Morse and Mackenzie, 1990). The model simulations

BGD
9, 8475–8539, 2012

predict that pH decreases with depth below the water-sediment interface as a result of CO_2 generation (results not shown). This is accompanied by a decrease in $[CO_3^{2-}]$ and $CaCO_3$ saturation. However, the point where the porewater becomes undersaturated depends on the imposed boundary conditions. The relationship between POC oxidation and PIC dissolution is further complicated by the presence of three $CaCO_3$ phases with differing solubilities and dissolution kinetics. As a result, no simple relationship emerges between the PIC:POC deposition ratio and PIC dissolution: each PIC phase needs to be considered separately. Overall, the depth-resolved saturation state calculations are in line with the observations of Mucci et al. (2000) who reported a rapid decrease with depth of pore water saturation state with respect to aragonite, and occasionally with respect to calcite, in continental sediments of the Eastern Canadian continental margin.

For the shallow environments containing Mg-calcite (reefs and banks and bays), dissolution of this most soluble phase begins when the POC deposition flux exceeds $\sim 0.8\,\mathrm{mol\,C\,m^{-2}\,yr^{-1}}$ (Fig. 2a). Beyond this point, the depth-integrated dissolution rate of Mg calcite increases linearly with additional POC deposition. For the shelves, aragonite will begin to dissolve when the POC flux exceeds $\sim 0.5\,\mathrm{mol\,C\,m^{-2}\,yr^{-1}}$, and then increase linearly with additional POC deposition, until all aragonite is exhausted on the "carbonate" and "non-carbonate" shelves; at this point the dissolution flux equals the imposed deposition flux of aragonite (Fig. 2b). For the reefs, there is minimal aragonite dissolution, as the sediment is buffered by Mg-calcite dissolution. In the banks and bays environment, some aragonite dissolution is observed at the highest POC fluxes. Calcite dissolution is not observed for the reefs or banks and bays environments (Fig. 2c). While calcite is never completely dissolved on the "carbonate" shelves, complete dissolution occurs at the highest POC loadings for the 25 m water depth "non-carbonate" shelves.

Assuming a dry sediment density of $2.5\,\mathrm{g\,cm^{-3}}$, the model-predicted average PIC content of coastal sediments at 20 cm below the SWI (the depth by which the vast majority of reactive POC is degraded) is 0.4 % for the "non-carbonate" shelves, 2.2 %

BGD
9, 8475–8539, 2012

for the "carbonate" shelves, 26 % in banks and bays, and 90 % below reefs. The corresponding PIC contents are 0, 0.26, 3.1, and 11 weight % C, respectively. In the baseline simulations, on average 45 % of the deposited PIC is dissolved on "carbonate" shelves, 76 % on "non-carbonate" shelves, 16 % in banks and bays, and 4 % in reef environments (Fig. 1a). Although the model assumes that PIC deposition does not depend on SFD within the coastal zone (Sect. 2.4.1), the bottom water carbonate saturation states (Ω) decreases with water depth while metabolically-induced PIC dissolution also decreases with water depth, due to decreased POC deposition flux. The net result is that the model-predicted PIC concentrations are higher at greater seafloor depth on the shelves (0.22 % C_{inorg} at 25 m water depth vs. 0.30 % C_{inorg} at 150 m water depth for "carbonate" shelves), because of lower dissolution. For comparison, Mucci et al. (2000) report PIC concentrations on the order of 0.4–0.9 wt %. C_{inorg} in sediments accumulating between 230 to 360 m water depth on the continental shelf of Eastern Canada.

The production of DIC from PIC dissolution is significantly smaller than that due to POC mineralization (Fig. 1A). Carbonate dissolution represents 3.2–7.8 % of the total DIC generated in "non-carbonate" shelf sediments (depending on SFD), 4.6 %–9.5 % of total DIC production in "carbonate" shelf sediments, and 11 % and 10 % of DIC production in sediments of banks and bays and reefs, respectively.

3.1.3 Organic matter degradation: alkalinity production

Except for organic carbon oxidation coupled to aerobic respiration, the primary redox reactions generate alkalinity, while secondary redox reactions generally consume alkalinity (Table 3). On a per mole basis, oxidation of reduced iron (R8 in Table 3) consumes exactly the amount of alkalinity generated by iron reduction (R5), hence in Fig. 1b net iron reduction (= R5–R8) is reported. We further define net sulfate reduction as sulfate reduction (R6) minus sulfide oxidation (R9) and FeS oxidation (R10). Although the latter reaction (R10) by itself does not consume alkalinity (Table 3), precipitation of FeS (R14) results in the production of 2 fewer alkalinity equivalents than would be expected

BGD
9, 8475–8539, 2012

from the iron and sulfate reduction reactions (see Sect. 2.5); therefore, HS^- that combines with Fe^{2+} but which is subsequently re-oxidized to sulfate consumes the same amount of alkalinity as if it were oxidized directly from the aqueous form (R9).

The effect of the nitrogen cycle on sediment alkalinity production is slightly more complicated. First, denitrification (R4) is a source of alkalinity. Second, ammonification during hydrolysis (Sect. 2.3.1) also generates alkalinity (R1, R2) but, if followed by nitrification (R7), the coupled process becomes a net alkalinity sink. That is, if all NH_4^+ generated by ammonification is nitrified, 0.16 equivalent of alkalinity would be consumed per mole of POC hydrolyzed. In what follows, we therefore opt to separately report the alkalinity production due to net ammonification (ammonification – nitrification) and denitrification.

Net sulfate reduction is by far the greatest contributor (70–82 %) of in situ alkalinity generation (Fig. 1b). Net ammonification contributes 4.2–9.0 % of the overall alkalinity, while denitrification yields 1.4–3.6 % and net iron reduction 1.0–2.8 %. The relative contribution of sulfate reduction is greatest at the shallow water depths, where reactive POC deposition is higher. Ammonification is directly proportional to the POC deposition flux, decreasing with water depth. Despite the fact that the percentage of C oxidized via nitrate reduction increases with water depth, the overall amount of denitrification decreases along with the decrease in reactive POC flux with depth. Alkalinity production by net iron reduction is dictated by the reactive iron influx, which we scale to sedimentation rate, and hence it decreases (in absolute value) with water depth.

3.1.4 Carbonate dissolution: alkalinity production

Carbonate mineral dissolution is the second largest contributor after sulfate reduction to in situ alkalinity generation (Fig. 1b). It accounts for 6 to 20 % of alkalinity production. It is highest in sediments from reefs and banks and bays, the two environments for which Mg-calcite is included as a carbonate mineral phase. In the baseline scenario, aragonite dissolves completely in sediments of carbonate and non-carbonate shelves (Fig. 1a). Depending on seafloor depth, dissolution consumes 60–70 % of deposited

BGD
9, 8475–8539, 2012

calcite on the non-carbonate shelves, and 8–25 % on the carbonate shelves. In sediments from banks and bays, 61 % of deposited Mg-calcite dissolves, 1 % of deposited aragonite, and none of the deposited calcite. For sediments accumulating below reefs, only Mg-calcite (16 %) dissolves (Fig. 1a).

Dissolution of 1 mol PIC generates 2 equivalents of alkalinity, which are added to the alkalinity generated by the redox reactions. PIC dissolution accounts for 9 to 19 % of alkalinity generated in "carbonate" shelf sediments (depending on water depth), 6 to 16 % in "non-carbonate" shelf sediments, and 19 % in sediments from banks and bays and reef environments (Fig. 1b).

3.1.5 Global coastal flux estimate

The fluxes for the various coastal environments defined by Milliman et al. (1996) are multiplied by their corresponding surface areas to estimate first-order areal-integrated coastal DIC fluxes (Table 7, Fig. 3). Because of their large areal extent, "non-carbonate" shelves contribute most (55 %) to global DIC generation. "Carbonate" shelves, banks and bays, and reef environments contribute 37 %, 5 %, and 3 %, respectively, to global coastal benthic DIC release (Table 7, Fig. 3a). As discussed earlier, benthic DIC fluxes are largely sustained by benthic organic carbon degradation, while carbonate dissolution only contributes a small fraction. Global organic carbon oxidation in coastal sediments amounts to 117 $\mathrm{Tmol\,yr^{-1}}$, of which 56 % occurs on 'non-carbonate' shelves, 37 % on "carbonate" shelves, 4 % in banks and bays, and 3 % in reef environments. Results show the large dominance of anaerobic decomposition of POC for DIC production and fluxes. Sulfate reduction accounts for 83 % of reactive POC oxidized on the shelves, 85 % in banks and bays, and 81 % of org C oxidation in reefs. Globally (i.e. all environments combined), 83 % of organic C oxidation in coastal sediments is coupled to sulfate reduction. While the inferred dominant role of sulfate reduction contrasts with lower contributions proposed in earlier work (Jørgensen, 1982; Canfield, 1989; Archer et al., 2002), it is in line with the more recent work of Canfield (2005) and Thullner et al. (2009). The baseline simulations further yield global contributions to

BGD
9, 8475–8539, 2012

organic carbon oxidation of 14, 3 and 0.4 % for aerobic respiration, denitrification, and dissimilatory iron reduction, respectively. For the baseline case, the model calculations predict that 6.8 Tmol of PIC dissolve annually, which corresponds to 28, 30, and 30 % of the coastal deposition fluxes of calcite, aragonite and Mg-calcite, respectively (Table 7). Carbonate dissolution contributes approximately 6 % and 4 % of the total DIC flux from "carbonate" and "non-carbonate" shelf sediments, respectively, 11 % of the DIC from bank and bay sediments, and 10 % of the DIC from reefs. Globally, therefore, about 5 % of DIC release from coastal sediments (7 Tmol yr^{-1}, Table 7) results from PIC dissolution.

In all the coastal environments, net sulfate reduction (NSR) and PIC dissolution dominate alkalinity generation (Fig. 3b). The share of in situ alkalinity generated via NSR is greatest where POC oxidation is high and PIC dissolution is relatively low: it accounts for 82 % of alkalinity generated at the 25 m depth on "non-carbonate" shelves, while PIC dissolution contributes 6 %. Overall, on "non-carbonate" shelves, NSR is responsible for 79 % of the alkalinity generated, and PIC dissolution contributes 9 %. For "carbonate" shelves, NSR and PIC dissolution contribute 77 % and 11 %, respectively, to A_T generation. In both the reef and "banks and bays" environments, NSR contributes 70 % of in situ alkalinity, while PIC dissolution contributes 20 %. Net ammonification is related to reactive POC deposition, and therefore its contribution to A_T is highest where POC deposition is greatest (9 %) in "banks and bays" and the 25 m depth of both carbonate and non-carbonate shelves, and lowest at the 150 m depth on the shelves (4 %). Denitrification and net iron reduction each contribute approximately 1–2 % of in situ alkalinity generation in each of the environments. On a global scale, in situ alkalinity generation by sediment processes in the coastal zone is largely dominated by net sulfate reduction (78 %), followed by PIC dissolution (11 %), net ammonification (7.7 %), denitrification (2.1 %) and net iron reduction (1.5 %). Total alkalinity generation equals 124 Teq yr^{-1} (Fig. 4b).

The effective alkalinity flux to the water column, A_T^* (Sect. 2.5), is much smaller than the in situ alkalinity generation, because the burial of reduced sulfur is small and, thus,

BGD
9, 8475–8539, 2012

almost all H_2S+HS^- is reoxidized in the water column. In other words, while sulfate reduction is the major source of in situ alkalinity generation, it contributes little to A_T^* (Fig. 3b). Note, however, that sulfate reduction indirectly affects A_T^* through its influence on the rates of other redox processes and PIC dissolution. PIC dissolution contributes most to A_T^*, accounting for 65 % of the effective benthic alkalinity efflux from reefs and banks and bays, 49 % on "carbonate" shelves, and 42 % on "non-carbonate" shelves. Net ammonification contributes 23 % of A_T^* in reefs, 26 % in banks and bays, 32 % in "carbonate" shelves, and 39 % of A_T^* on "non-carbonate" shelves. Globally (i.e. all coastal environments combined, PIC dissolution releases 13.5 Teq yr^{-1} of A_T^* (47 %) and net ammonification 9.6 Teq yr^{-1} (33 %). Denitrification, net iron reduction and reduced S burial contribute 9.0 %, 6.6 % and 5.7 %, respectively (Table 7).

For the baseline reactive POC deposition flux (117 Tmol yr^{-1}), the model predicts an effective alkalinity flux A_T^* from coastal sediments of 29 Teq yr^{-1}. This value agrees with Chen's (2002) range of 16–31 Teq yr^{-1}, although the latter was estimated through a very different approach. The proposed benthic alkalinity source of 29 Teq yr^{-1} is also approximately equal to the 30 Teq yr^{-1} of alkalinity supplied to the oceans by rivers (Suchet et al., 2003). According to our calculations, PIC burial in coastal sediments represents an alkalinity sink of 32.5 Teq yr^{-1}. The corresponding PIC dissolution flux (6.75 Tmol yr^{-1}) is comparable to the 6 Tmol yr^{-1} predicted by Andersson et al. (2003), although the latter dissolution flux was obtained for a much lower reactive POC deposition flux of 40 Tmol yr^{-1}. With a reactive POC deposition flux of 40 Tmol yr^{-1}, our model would yield a significantly lower PIC dissolution (~2 Tmol yr^{-1}, see below).

3.2 Sensitivity analyses

3.2.1 Sulfur cycling

Sensitivity analyses with respect to internal model parameters are performed for the 75 m water depth carbonate shelf sediments. An increase in the sulfide oxidation rate

BGD
9, 8475–8539, 2012

constant, k_{SulfO_x}, increases the in situ sulfur recycling. As a result, 10-, 100-, and 1000-fold increases in k_{SulfO_x} increase the contribution of sulfate reduction to POC oxidation to 82 %, 87 %, and 92 %, respectively, at the expense of the other C oxidation pathways (Fig. 5a). Despite its very small relative contribution to the carbon decomposition, the accompanying declines in iron reduction cause porewater pH to drop to lower values (see also Jourabchi et al., 2005), and hence enhances calcite dissolution (by 82 % for a 1000-fold increase in k_{SulfO_x}).

Faster sulfide oxidation markedly reduces net sulfate reduction (Fig. 5b), but also decreases oxygen availability for other secondary redox reactions, particularly nitrification. This in turn has a significant effect on alkalinity, as nitrification consumes alkalinity (Table 3). The combination of increased calcite dissolution and increased net ammonification results in a 24 % increase in A_T^* with a 1000 times higher than baseline value of k_{SulfO_x} (Fig. 5b). Decreasing bioirrigation of sulfides (only) by 90 % increases pyrite burial by 16 % and calcite dissolution by 143 % , leading to a 7 % increase in A_T^*. The results thus illustrate that the in situ fate of the sulfide produced by sulfate reduction can have a significant indirect effect on the effective benthic flux of alkalinity, even though the efflux of H_2S+HS^- is explicitly excluded in the definition of A_T^*.

3.2.2 Iron cycling

In our model, a doubling of the imposed reactive Fe(III) deposition flux for the 75 m water depth carbonate shelf sediments approximately doubles the rates of all iron-related reactions, including iron reduction and pyritization (Fig. 5b). It causes an 81 % increase in pyrite burial, prevents calcite dissolution (due to higher pH), and increases A_T^* by 1 %. Pyrite burial can also be enhanced by increasing the rate constant for FeS precipitation. For a 10-fold increase of the rate constant k_{FeS}, the contribution of pyrite burial to A_T^* increases by 67 %, while the Fe^{2+} efflux drops by 41 %. As with sulfur, changes in iron cycling within the sediments have a measurable effect on the benthic

BGD
9, 8475–8539, 2012

flux of alkalinity to the water column, but they hardly affect the efflux of DIC, because POC mineralization dominates DIC production in the sediments.

3.2.3 Carbonate dissolution

An increase of the rate constant for the PIC dissolution by 50 % leads to a 21 % increase in calcite dissolution (aragonite is already completely dissolved at 75 m on "carbonate" shelves), resulting in a 2 % increase in A_T^* (Fig. 5b). Decreasing the dissolution kinetics by 50 % decreases calcite dissolution by 32 % (no effect on aragonite dissolution); yet this effect on A_T^* is also small (3 % decrease).

3.3 Response of coastal DIC and ALK fluxes to global change

3.3.1 Global sensitivity to coastal productivity changes

Estimates of reactive POC deposition flux in the coastal zone vary by more than an order of magnitude, with our baseline estimate being at the high end of the range (Table 1). Here, we test the sensitivity of DIC and alkalinity fluxes to changes in the reactive POC deposition flux that range from 12.5 % to 150 % of the baseline flux (Fig. 4a). As expected, the model outcomes are highly sensitive to the reactive POC deposition flux (Fig. 4, Table 8). As the reactive POC deposition flux increases, the absolute rates of all the primary redox pathways coupled to organic C oxidation increase, except for iron reduction, which decreases because the reactive iron(III) deposition flux is fixed and Fe^{2+} reoxidation decreases, hence slowing down the internal iron redox cycle (Fig. 4a). The percentage of organic carbon oxidized via sulfate reduction grows from 45 % to 86 % of total POC oxidation, while the percentage of iron reduction drops sharply. At the same time, the relative contributions of aerobic respiration, denitrification, and PIC dissolution to DIC production progressively decrease (Fig. 6a).

Carbonate dissolution contributes a small amount of the benthic DIC efflux, compared to POC oxidation (Fig. 6a). According to our model calculations, PIC dissolution

BGD
9, 8475–8539, 2012

starts when the reactive POC deposition flux exceeds 30 Tmol yr^{-1}. For the lowest POC deposition flux considered in the sensitivity runs (12.5 % of baseline flux), the porewaters remain supersaturated with respect to all the carbonate mineral phases considered in this study (Fig. 4a), with the exception of aragonite in the 150 m water depth shelf sediments (results not shown). Increasing POC deposition flux increases PIC dissolution (Fig. 7). Globally, 30 % of the PIC deposited along the continental margins dissolves in the baseline scenario, mostly on the shelves. The remaining PIC is concentrated on reefs and banks and bays, where a small amount of dissolution is sufficient for the pore waters to reach saturation, hence allowing the carbonate minerals to be buried. With the estimated baseline deposition fluxes, Mg-calcite is a minor contributor to DIC generation. With increasing organic matter oxidation, the aragonite dissolution flux increases up to 3.1 Tmol yr^{-1} when the reactive POC deposition flux reaches 50 % of the baseline value, at which point aragonite is essentially depleted on the shelves. At higher POC deposition fluxes, calcite starts to dissolve. Overall, PIC dissolution levels out at the higher POC deposition fluxes tested, because of the depletion of carbonate phases in shelf sediments, which make up nearly 95 % of the coastal area (Figs. 7 and 8b).

Despite the complex interplay of processes controlling alkalinity generation and efflux, A_T^* increases nearly linearly with the reactive POC deposition flux (Figs. 4b and 8a). At low POC deposition fluxes, when PIC dissolution is minimal, redox processes (particularly iron reduction) and sulfide burial are the main source of A_T^* (Fig. 6b). With increasing POC deposition, increased sulfate reduction and the resulting increase in sulfide re-oxidation decreases oxygen availability for other oxygenation reactions. Therefore, aerobic respiration, iron reduction, and nitrification all decrease. Aerobic C oxidation has no effect on alkalinity, and *net* iron reduction is fixed by the reactive iron deposition flux. In contrast, the decrease in nitrification, coupled to the increase in deposition of organic nitrogen associated with POC, leads to an increase in net ammonification (Figs. 4b and 6b), which is the second largest contributor to A_T^* (after PIC dissolution) in the baseline simulations.

BGD
9, 8475–8539, 2012

Because the simulation results are most sensitive to the reactive POC deposition flux, it is possible to express the effluxes of DIC and A_T^* in terms of this forcing. Over the range of POC deposition fluxes tested, the global coastal DIC efflux can thus be approximated by (Fig. 8a):

$$J_{DIC\_out}(\mathrm{Tmol\,yr^{-1}}) = 126 + 0.039(J_{POC} - 117) \quad (18)$$

For the same range of reactive POC deposition fluxes, the effective benthic alkalinity flux (A_T^*) can also be approximated by a linear function (Fig. 8b):

$$A_T^*(\mathrm{Teq\,yr^{-1}}) = 29 + 0.217(J_{POC} - 117) \quad (19)$$

where in both equations J_{POC} is expressed in $\mathrm{Tmol\,C\,yr^{-1}}$.

3.3.2 Global sensitivity to ocean acidification

An increase in bottom water DIC by 5 %, which roughly corresponds to a 300 ppm increase in atmospheric CO_2 and a corresponding drop in the baseline water column pH of 0.24 units, increases carbonate mineral dissolution from 6.8 $\mathrm{Tmol\,yr^{-1}}$ in the baseline scenario to 9 $\mathrm{Tmol\,yr^{-1}}$ (Table 8). In contrast, the reduction in bottom water pH has only a marginal impact on the various redox pathways considered in the model. Consequently, under the high atmospheric CO_2 scenario, the model-predicted benthic DIC efflux only increases by 1.5 %, but A_T^* increases by 17 %. That is, the sediments release an additional 4.4 $\mathrm{Teq\,yr^{-1}}$ of alkalinity in response to the acidification of the coastal waters (Fig. 5).

Decreasing the PIC deposition flux by 56 %, to simulate reduced calcification triggered by ocean acidification, decreases PIC dissolution by 2.1 $\mathrm{Tmol\,yr^{-1}}$ (31 % drop relative to baseline value) globally, resulting in a 4.2 $\mathrm{Teq\,yr^{-1}}$ decrease in A_T^* (i.e., a drop of 15 % compared to the baseline). This is primarily accompanied by PIC depletion on the shelves. Under the baseline scenario, aragonite completely dissolves on both

BGD
9, 8475–8539, 2012

the carbonate and non-carbonate shelves, while only 30 % of shelf-deposited calcite dissolves. With the imposed decreased PIC deposition, 100 % of the calcite on the non-carbonate shelves dissolves as well, hence the corresponding sediments can no longer provide any additional buffering. The loss of buffering capacity of shelf sediments is not compensated by carbonate dissolution in the other benthic environments and, as a result, A_T^* drops significantly. Note that the decrease in A_T^* predicted for the reduced PIC deposition scenario (4.2 Teq yr^{-1}) is of the same magnitude as the increase in A_T^* predicted for the high water column DIC scenario (4.4 Teq yr^{-1}). Thus, the response of coastal sediments to ocean acidification is expected to be similarly sensitive to changes in water column pH and calcification, within their projected ranges for the coming decades.

4 Model limitations

The present model approach adopts a very coarse representation of the global coastal ocean, dividing the total coastal seafloor area of 2×10^7 km^2 into merely four characteristic environments as described by Milliman and Droxler (1996), which are characterized by an average depth or further subdivided into three depth intervals. By averaging over such large areas, many local diagenetic features cannot be captured. The main reasons behind the approach chosen here are the scarcity and resolution of the observational data and, in particular, our current inability to constrain boundary conditions and model parameters at a finer areal resolution. In this context, the lack of higher resolution estimates of organic matter deposition fluxes and reactivity in the heterogeneous and dynamic global coastal ocean is by far the most important limitation towards a finer-scale regionalization of benthic C fluxes. Nevertheless, the sensitivity analysis with respect to internal model parameters and changes in organic matter deposition fluxes helps quantify the uncertainty in global flux estimates that is associated with the inability to resolve the dynamics at a finer spatial scale. Previously published estimates of the global POC deposition flux (Table 1) yield an average value

BGD
9, 8475–8539, 2012

of ~90 Tmol yr^{-1} and, therefore, our baseline simulation with a reactive POC deposition flux of 117 Tmol yr^{-1} and a total flux of 140 Tmol yr^{-1} should be viewed as an upper bound estimate for DIC and A_T^* fluxes. The results of the sensitivity study indicate that, for the bulk range of 60–120 Tmol yr^{-1} (±30 % of the average value), the predicted global coastal ocean flux of A_T^* is most likely constrained within a factor of 2 (Fig. 4b). Over this POC flux range, degradation driven dissolution of shallow water carbonates generates ~4–7 Tmol yr^{-1} of A_T^*, while the total irreversible buffering source of alkalinity from shallow marine sediments (PIC dissolution, denitrification and sulfur burial) is on the order of 11–19 Tmol yr^{-1}. Taking the contribution of net ammonification and net iron reduction, A_T^* fluxes increase to 16–29 Tmol yr^{-1} (Fig. 4b). In contrast, the uncertainty in key internal model parameter values has little influence on the uncertainty in estimated A_T^* fluxes for a given POC flux (Fig. 5b). Similarly, boundary conditions such as bottom water oxygen, nitrate, DIC or temperature only exert a second-order influence on A_T^* estimates. In particular, temperature effects are small because they only result from temperature-induced changes in diffusion coefficients, equilibrium constants, and the solubility of the carbonate phases, but ignore the effect of temperature on organic matter decomposition, which is the main driver of PIC dissolution and A_T^* generation. However, explicitly accounting for the effect of temperature on primary redox reactions is not straightforward. These processes proceed via multiple enzymatic reactions resulting from the combined effort of billions of individual microorganisms and involving a number of different oxidants and intermediate compounds. Therefore, factors such as physiological adaption, selective pressure and the exact reaction path also play an important role in determining the effect of temperature. Observations show that the dominant microbial populations in each environment are optimally adapted to the prevailing environmental conditions and mineralization rates in permanently cold Arctic sediments are similar to that of temperate nearshore environments (Arnosti et al., 1998; Kostka et al., 1999; Jørgensen, 2006). Finally, uncertainties in flux estimates may arise because some of the assumptions made regarding transport processes may not be appropriate for modeling non-accumulating permeable sands. There is very little

BGD
9, 8475–8539, 2012

information on carbon fluxes from such sediments (Reimers et al., 2004; Jahnke, 2005; Rusch, 2006). Nevertheless, the few studies reveal a significant potential for organic oxidation and DIC release from these environments and further attention should thus be given to these settings in the future.

Any attempt to infer the global coastal benthic dynamics from the currently limited observational data set should be viewed as a work in progress that requires constant reevaluation and testing in the context of our evolving mechanistic understanding of this environment. Nevertheless, our modeling study provides a first-order global estimate of the coupled carbon dynamics in coastal sediments and of the associated benthic DIC and alkalinity fluxes. It also reveals knowledge and data gaps in our global understanding of DIC and alkalinity fluxes in the global ocean and unravels the sensitivity of the coastal carbon cycling to ongoing global change.

5 Synthesis

A one-dimensional reactive transport model (RTM) of early diagenesis is used to describe primary and secondary redox reactions and their impact on the dissolution of carbonate mineral phases (calcite, aragonite, and 15 % Mg-calcite) in shallow marine sediments. The model predictions are extrapolated to estimate benthic fluxes of DIC and alkalinity for the global coastal ocean, based on the benthic typology proposed by Milliman and Droxler (1996). However, because our baseline scenario falls in the higher range of global coastal POC deposition fluxes reported in the literature, the absolute flux values should be viewed as upper-bound estimates. The results highlight the dominant role of anaerobic respiration, mainly sulfate reduction, in the decomposition of sediment organic matter and, hence, as a source of benthic DIC in the coastal ocean (77 % of the baseline DIC efflux of 126 Tmol yr^{-1}). The oxidation of organic carbon is estimated to cause the dissolution of approximately 7 Tmol yr^{-1} of shallow-water marine carbonate minerals (circa 0.1 Pg C yr^{-1}). As expected, the predicted carbonate dissolution flux is very sensitive to the supply of reactive organic matter to the sediments. For

BGD
9, 8475–8539, 2012

an increase of the reactive POC deposition flux by a factor 1.5, carbonate dissolution increases by about 20 %.

For the baseline reactive POC deposition flux of 117 Tmol yr^{-1} (total POC deposition flux of 140 Tmol yr^{-1}), the model-derived total alkalinity efflux from the sediments is 120 Teq yr^{-1}. A large fraction of this efflux is under the form of reduced solutes that are highly unstable in oxygenated waters and, therefore, are unlikely to serve as buffer against rising atmospheric CO_2 and ocean acidification. By assuming that free sulfide reaching the sediment-water interface is instantaneously and quantitatively oxidized, the effective benthic alkalinity flux to the water column (A_T^*) is 29 Teq yr^{-1}. The two main contributions to A_T^* are carbonate dissolution (46 %) and net ammonification (33 %), with smaller contributions from denitrification (9 %), net iron reduction (7 %), and reduced sulfur burial (6 %). Subtracting net ammonification from A_T^* results in a minimum estimate of the effective benthic alkalinity supply to the global coastal ocean on the order of 19 Teq yr^{-1}.

While our estimate of the effective benthic alkalinity flux A_T^* of 29 Teq yr^{-1} compares well with the range of 16 to 31 Teq yr^{-1} proposed by Chen (2002) for the coastal ocean, our analysis of the underlying sedimentary processes is quite different. Chen and Wang (1999) attribute over 80 % of the benthic alkalinity flux to iron and sulfate reduction, with no contribution from carbonate mineral dissolution. Our analysis is thus more in line with that of Berelson et al. (2007), who acknowledge the production of alkalinity by carbonate dissolution, along with sulfate reduction and the reoxidation of sulfide by iron oxides. These authors report an average alkalinity efflux from California margin sediments of about 2.5 meq m^{-2} d^{-1}, which is close to the average A_T^* flux we calculate for carbonate and non-carbonate shelf sediments (~2.8 meq m^{-2} d^{-1}). In contrast, Hu and Cai (2011) report a significantly lower flux of alkalinity (4–5 Teq yr^{-1}) generated by ocean margin sediments. Their estimate only takes into account net benthic denitrification and pyrite burial, because the authors implicitly treat the coastal water column plus the underlying sediments as a single system and, hence, alkalinity-producing benthic processes that are (or could be) counteracted by alkalinity-consuming processes

BGD
9, 8475–8539, 2012

in the water column are not considered. The authors also do not include carbonate precipitation and dissolution because their focus is on anaerobic processes. Using this whole-coastal ocean approach, yet focusing only on anaerobic processes, leads Hu and Cai to omit the two major sources of A_T^* included in our model: carbonate dissolution and ammonification. Once the differences in system delineation (whole ocean versus sediments, anaerobic processes only vs. coupled redox and dissolution) are recognized, the alkalinity fluxes assigned by Hu and Cai to denitrification (1.5 Teq yr^{-1}) and pyrite burial (2.4–3.3 Teq yr^{-1}) are nevertheless comparable to our baseline estimates of 2.6 Teq yr^{-1} for coastal zone denitrification, and 1.6 Teq yr^{-1} for reduced sulfur burial.

Despite the diversity of approaches, relatively coherent estimates of the contribution of sediment biogeochemical processes to benthic DIC and alkalinity fluxes in nearshore and continental shelf environments are emerging. With the early diagenetic modeling approach used here, it is further possible to analyze the sensitivity of the benthic fluxes to external forcings and model parameters. This strengthens our ability to predict the response of benthic DIC and alkalinity fluxes from coastal sediments to anthropogenic perturbations, in particular coastal eutrophication and ocean acidification.

Supplementary material related to this article is available online at: http://www.biogeosciences-discuss.net/9/8475/2012/bgd-9-8475-2012-supplement.pdf.

Acknowledgement. This work is a contribution to the "European Project on Ocean Acidification" (EPOCA) which received funding from the European Community's Seventh Framework Programme (FP7/2007-2013) under grant agreement n° 211384. It has been supported by the government of the Brussels-Capital Region (Brains Back to Brussels award to PR), by the Netherlands Organization for Scientific Research (NWO) (VIDI award to PR) and by the National Environment Research Council (NERC Fellowship to SA).

BGD
9, 8475–8539, 2012

References

Aguilera, D. R., Jourabchi, P., Spiteri, C., and Regnier, P.: A knowledge-based reactive transport approach for the simulation of biogeochemical dynamics in Earth systems, Geochem. Geophy. Geosy., 6, Q07012, 2005.

Andersson, A. J., Mackenzie, F. T., and Ver, L. M.: Solution of shallow-water carbonates: an insignificant buffer against rising atmospheric CO_2, Geology, 31, 513, 2003.

Andersson, A. J., Mackenzie, F. T., and Lerman, A.: Coastal ocean and carbonate systems in the high CO_2 world of the Anthropocene, Am. J. Sci., 305, 875–918, 2005.

Andersson, A. J., Mackenzie, F. T., and Gattuso, J. P.: Effects of ocean acidification on benthic processes, organisms, and ecosystems, in: Ocean Acidification, edited by: J.-P. Gattuso and L. Hansson, Oxford University Press, Oxford, pp. 122, 2011.

Anggara Kasih, G., Chiba, S., Yamagata, Y., Shimizu, Y., and Haraguchi, K.: Modeling early diagenesis of sediment in Ago Bay, Japan: a comparison of steady state and dynamic calculations, Ecol. Model., 215, 40–54, 2008.

Archer, D. E., Morford, J. L., and Emerson, S. R.: A model of suboxic sedimentary diagenesis suitable for automatic tuning and gridded global domains, Global Biogeochem. Cy., 16, 1017, 2002.

Archer, D., Eby, M., Brovkin, V., Ridgwell, A., Cao, L., Mikolajewicz, U., Caldeira, K., Matsumoto, K., Munhoven, G., and Montenegro, A.: Atmospheric lifetime of fossil fuel carbon dioxide, Annu. Rev. Earth Planet Sci., 37, 117–134, 2009.

Arndt, S., Regnier, P., Goddéris, Y., and Donnadieu, Y.: GEOCLIM reloaded (v 1.0): a new coupled earth system model for past climate change, Geosci. Model Dev., 4, 451–481, doi:10.5194/gmd-4-451-2011, 2011.

Arnosti, C., Jørgensen, B. B., Sageman, J., and Thamdrup, B.: Temperature dependence of microbial degradation of organic matter in marine sediments: polysaccharide hydrolysis, oxygen consumption, and sulfate reduction, Mar. Ecol. Prog. Ser., 165, 59–70, 1998.

Berelson, W. M., Balch, W. M., Najjar, R., Feely, R. A., Sabine, C., and Lee, K.: Relating estimates of $CaCO_3$ production, export, and dissolution in the water column to measurements of $CaCO_3$ rain into sediment traps and dissolution on the sea floor: a revised global carbonate budget, Global Biogeochem. Cy., 21, GB1024, 2007.

Berg, P., Rysgaard, S., and Thamdrup, B.: Dynamic modeling of early diagenesis and nutrient cycling, a case study in an artic marine sediment, Am. J. Sci., 303, 905–955, 2003.

BGD
9, 8475–8539, 2012

Berner, R. A.: Burial of organic carbon and pyrite sulfur in the modern ocean: its geochemical and environmental significance, Am. J. Sci., 282, 451–473, 1982.
Blair, N. E. and Aller, R. C.: Anaerobic methane oxidation on the Amazon shelf, Geochim. Cosmochim. Ac., 59, 3707–3715, 1995.
Boudreau, B. P.: Is burial velocity a master parameter for bioturbation?, Geochim. Cosmochim. Ac., 58, 1243–1249, 1994.
Boudreau, B. P.: Diagenetic models and their implementation: modelling transport and reactions in aquatic sediments, Springer-Verlag, Berlin, 1996.
Boudreau, B. P. and Canfield, D. E.: A Comparison of Closed-and Open-System Models for Porewater pH and Calcite-Saturation State, Geochim. Cosmochim. Ac., 57, 317–334, 1993.
Bosence, D. W. J., Royston, J. R., and Quine, M. L.: Sedimentology and budget of a recent carbonate mount, Florida Keys, Sedimentology, 3, 317–343, 1985.
Burdige, D. J.: The kinetics of organic matter mineralization in anoxic marine sediments, J. Mar. Res., 49, 727–761, 1991.
Burdige, D. J., Hu, X., and Zimmerman, R. C.: The widespread occurrence of coupled carbonate dissolution/reprecipitation in surface sediments on the Bahamas Bank, Am. J. Sci., 310, 492–521, 2010.
Canfield, D. E.: Sulfate reduction and oxic respiration in marine sediments: implications for organic carbon preservation in euxinic environments, Deep-Sea Res., 36, 121–138, 1989.
Canfield, D. E.: The sulfur cycle, Aq. Geomicrobiol. Adv. Mar. Biol., 48, 313–381, 2005.
Caldeira, K. and Wickett, M. E.: Anthropogenic carbon and ocean pH, Nature, 425, 365–365, 2003.
Carignan, R. and Tessier, A.: The co-diagenesis of sulfur and iron in acid lake sediments of Southwestern Quebec, Geochim. Cosmochim. Ac., 52, 1179–1188. 1988.
Centler, F., Shao, H., De Biase, C., Park, C. H., Regnier, P., Kolditz, O., and Thullner, M.: GeoSysBRNS – a flexible multidimensional reactive transport model for simulating biogeochemical subsurface processes, Comput. Geosci., 36, 397–405, 2010.
Chen, C. T. A.: Shelf- vs. dissolution-generated alkalinity above the chemical lysocline, Deep-Sea Res. Pt. II, 49, 5365–5375, 2002.
Chen, C. T. A. and Wang, S. L.: Carbon, alkalinity and nutrient budgets on the East China Sea continental shelf, J. Geophys. Res., 104, 20675–20686, 1999.
Chen, C. T. A., Liu, K. K., and MacDonald, R.: Continental margin exchanges, in: Ocean Biogeochemistry, Springer-Verlag, Berlin, 53–97, 2003.

BGD
9, 8475–8539, 2012

Cloern, J. E.: Our evolving conceptual model of the coastal eutrophication problem, Mar. Ecol. Prog. Ser., 210, 53, 2001.
Dale, A. W., Regnier, P., Knab, N. J., Jorgensen, B. B., and Van Cappellen, P.: Anaerobic oxidation of methane (AOM) in marine sediments from the Skagerrak (Denmark): II. Reaction-transport modeling, Geochim. Cosmochim. Ac., 72, 2880–2894, 2008.
Dale, A. W, Brüchert, V., Alperin, M., and Regnier, P.: An integrated sulfur isotope model for Namibian shelf sediments, Geochim. Cosmochim. Ac., 73, 1924–1944, 2009.
Dulaiova, H., Ardelan, M. V., Henderson, P. B., and Charette, M. A.: Shelf-derived iron inputs drive biological productivity in the Southern Drake Passage, Global Biogeochem. Cy., 23, GB4014, 2009.
Dunne, J. P., Sarmiento, J. L., and Gnanadesikan, A.: A synthesis of global particle export from the surface ocean and cycling through the ocean interior and on the seafloor, Global Biogeochem. Cy., 21, 1-B4006, 2007.
Epping, E., van der Zee, C., Soetaert, K., and Helder, W.: On the oxidation and burial of organic carbon in sediments of the Iberian margin and Nazaré Canyon (NE Atlantic), Prog Oceanogr, 52, 399–431, 2002.
Feely, R. A., Sabine, C. L., Lee, K., Berelson, W., Kleypas, J., Fabry, V. J., and Millero, F. J.: Impact of anthropogenic CO_2 on the $CaCO_3$ system in the oceans, Science, 305, 362–366, 2004.
Gangstø, R., Gehlen, M., Schneider, B., Bopp, L., Aumont, O., and Joos, F.: Modeling the marine aragonite cycle: changes under rising carbon dioxide and its role in shallow water $CaCO_3$ dissolution, Biogeosciences, 5, 1057–1072, doi:10.5194/bg-5-1057-2008, 2008.
Hatcher, B. G.: Coral reef primary productivity. A hierarchy of pattern and process, Trends Ecol. Evol., 5, 149–155, 1990.
Henrichs, S. M. and Doyle, A. P.: Decomposition of 14 C-labeled organic substances in marine sediments, Limnol. Oceanogr., 765–778, 1986.
Hu, X. and Cai, W. J.: An assessment of ocean margin anaerobic processes on oceanic alkalinity budget, Global Biogeochem. Cy., 25, GB3003, 2011.
Jahnke, R. A.: The global ocean flux of particulate organic carbon: Areal distribution and magnitude, Global Biogeochem. Cy., 10, 71–88, 1996.
Jahnke, R. A.: Global synthesis, in: Carbon and Nutrient Fluxes in Continental Margins, Springer-Verlag, Berlin, 597–615, 2010.

BGD
9, 8475–8539, 2012

Jahnke, R. A., Craven, D. B. and Gaillard, J. F.: The influence of organic matter diagenesis on $CaCO_3$ dissolution at the deep-sea floor, Geochim. Cosmochim. Ac., 58, 2799–2809, 1994.
Jahnke, R., Richards, M., Nelson, J., Robertson, C., Rao, A., and Jahnke, D.: Organic matter remineralization and porewater exchange rates in permeable South Atlantic Bight continental shelf sediments, Cont. Shelf Res., 25, 1433–1452, 2005.
Joos, F., Plattner, G. K., Stocker, T. F., Marchal, O., and Schmittner, A.: Global warming and marine carbon cycle feedbacks on future atmospheric CO_2, Science, 284, 464, 1999.
Jørgensen, B. B.: A comparison of methods for the quantification of bacterial sulfate reduction in coastal marine sediments, Geomicrobiol. J., 1, 29–47, 1978.
Jørgensen, B. B.: Mineralization of organic-matter in the sea bed-the role of sulfate reduction, Nature, 296, 643–645, 1982.
Jørgensen, B. B.: Bacteria and marine biogeochemistry, in: Marine Geochemistry, edited by H. D. Schulz and M. Zabel, Springer, Berlin, 169–206, 2006.
Jørgensen, B. B. and Fenchel, T.: The sulfur cycle of a marine sediment model system, Mar. Biol., 24, 189–201, 1974.
Jourabchi, P., van Cappellen, P., and Regnier, P.: Quantitative interpretation of pH distributions in aquatic sediments: a reaction-transport modeling approach, Am. J. Sci., 305, 919–956, 2005.
Kaplan, I. R., Emery, K. O., and Rittenberg, S. C.: The distribution and isotopic abundance of sulphur in recent marine sediments off Southern California, Geochim. Cosmochim. Ac., 27, 297–312, 1963.
Katsev, S., Chaillou, G., and Sundby, B.: Effects of progressive oxygen depletion on sediment diagenesis and fluxes: a model for the lower St. Lawrence River Estuary, Limnol. Oceanogr., 52, 2555–2568, 2007.
Kleypas, J. A., Buddemeier, R. W., Eakin, C. M., Gattuso, J. P., Guinotte, J., Hoegh-Guldberg, O., Iglesias-Prieto, R., Jokiel, P. L., Langdon, C., and Skirving, W.: Comment on "Coral reef calcification and climate change: the effect of ocean warming", Geophys. Res. Lett., 32, L08601, 2005.
Koeve, W.: Upper ocean carbon fluxes in the Atlantic Ocean: the importance of the POC:PIC ratio, Global Biogeochem. Cy., 16, 1–17, 2002.
Kostka, J. E., Thamdrup, B., Glud, R. N., and Canfield, D. E.: Rates and pathways of carbon oxidation in permanently cold Arctic sediments, Mar. Ecol. Prog. Ser., 180, 7–21, 1999.
Land, L. S.: Diagenesis of skeletal carbonates, J. Sediment. Petrol., 37, 914–930, 1967.

BGD
9, 8475–8539, 2012

Lee, K., Tong, L. T., Millero, F. J., Sabine, C. L., Dickson, A. G., Goyet, C., Park, G. H., Wanninkhof, R., Feely, R. A., and Key, R. M.: Global relationships of total alkalinity with salinity and temperature in surface waters of the world's oceans, Geophys. Res. Lett., 33, L19605, 2006.

Luff, R. and Moll, A.: Seasonal dynamics of the North Sea sediments using a three-dimensional coupled sediment-water model system, Cont. Shelf Res., 24, 1099–1127, 2004.

Luff, R. and Wallmann, K.: Fluid flow, methane fluxes, carbonate precipitation and biogeochemical turnover in gas hydrate-bearing sediments at Hydrate Ridge, Cascadia Margin: numerical modeling and mass balances, Geochim. Cosmochim. Ac., 67, 3403–3421, 2003.

Mackenzie, F. T., Lerman, A., and Ver, L. M.: Role of the continental margin in the global carbon balance during the past three centuries, Geology, 26, 423–426, 1998.

Mackenzie, F. T., Andersson, A., Lerman, A., Ver, L. M.: Boundary exchanges in the global coastal margin: implications for the organic and inorganic carbon cycles, in: The Sea, Vol. 13, edited by: A. R. Robinson and K. H. Brink, Harvard University Press, Cambridge, 193–225, 2005.

Martens, C., Alperin, M., and Albert, D.: Deposition and fate of modern organic carbon in shelf/upper slope sediments near Cape Hatteras, North Carolina, Final Report, Department of Marine Sciences, University of North Carolina at Chapel Hill, Chapel Hill, NC 27599–3300, USA (US), 1998.

Meile, C., Berg, P., Van Cappellen, P., and Tuncay, K.: Solute-specific pore water irrigation: Implications for chemical cycling in early diagenesis, J. Mar. Res., 63, 601–621, 2005.

Middelburg, J. J., Soetaert, K., and Herman, P. M. J.: Empirical relationships for use in global diagenetic models, Deep-Sea Res. Pt. I, 44, 327–344, 1997.

Millero, F. J.: Thermodynamics of the carbon dioxide system in the oceans, Geochim. Cosmochim. Ac., 59, 661–677, 1995.

Milliman, J. D.: Production and accumulation of calcium carbonate in the ocean, budget of a nonsteady state, Global Biogeochem. Cy., 7, 927–957, 1993.

Milliman, J. D. and Droxler, A. W.: Neritic and pelagic carbonate sedimentation in the marine environment: ignorance is not bliss, Geol. Rundsch., 85, 496–504, 1996.

Mogollon, J. M., L'Heureux, I., Dale, A. W., and Regnier, P.: Methane gas-phase dynamics in marine sediments: a model study, Am. J. Sci., 309, 189, 2009.

BGD

9, 8475–8539, 2012

Mollenhauer, G. and Eglinton, T. I.: Diagenetic and sedimentological controls on the composition of organic matter preserved in California Borderland Basin sediments, Limnol. Oceanogr., 558–576, 2007.
Mollenhauer, G., Kienast, M., Lamy, F., Meggers, H., Schneider, R. R., Hayes, J. M., and Eglinton, T. I.: An evaluation of ^{14}C age relationships between co-occurring foraminifera, alkenones: and total organic carbon in continental margin sediments, Paleoceonography, 20, PA1016, 2005.
Morse, J. W. and Mucci, A.: Composition of carbonate overgrowths produced on Iceland spar calcite crystals buried in Bahamian carbonate-rich sediments, Sediment Geol., 40, 287–291, 1984.
Morse, J. W. and Mackenzie, F. T.: Geochemistry of Sedimentary Carbonates, Elsevier Science Ltd., Amsterdam, 1990.
Morse, J. W. and Eldridge, P. M.: A non-steady state diagenetic model for changes in sediment biogeochemistry in response to seasonally hypoxic/anoxic conditions in the "dead zone" of the Louisiana shelf, Mar. Chem., 106, 239–255, 2007.
Morse, J. W., Andersson, A. J., and Mackenzie, F. T.: Initial responses of carbonate-rich shelf sediments to rising atmospheric pCO_2 and "ocean acidification": Role of high Mg-calcites, Geochim. Cosmochim. Ac., 70, 5814–5830, 2006.
Mucci, A., Sundby, B., Gehlen, M., Arakaki, T., Zhong, S., and Silverberg, N.: The fate of carbon in continental shelf sediments of Eastern Canada: a case study, Deep-Sea Res. Pt. II, 47, 733, 2000.
Muller-Karger, F. E., Varela, R., Thunell, R., Luerssen, R., Hu, C., and Walsh, J. J.: The importance of continental margins in the global carbon cycle, Geophys. Res. Lett., 32, L01602, 2005.
Munhoven, G.: Glacial-interglacial rain ratio changes: implications for atmospheric CO_2 and ocean-sediment interaction, Deep-Sea Res. Pt. II, 54, 722–746, 2007.
Orr, J. C., Fabry, V. J., Aumont, O., Bopp, L., Doney, S. C., Feely, R. A., Gnanadesikan, A., Gruber, N., Ishida, A., and Joos, F.: Anthropogenic ocean acidification over the twenty-first century and its impact on calcifying organisms, Nature, 437, 681–686, 2005.
Palastanga, V., Slomp, C. P., and Heinze, C.: Long-term controls on ocean phosphorus and oxygen in a global biogeochemical model, Global Biogeochem. Cy., 25, GB3024, 2011.
Poulton, S. W. and Raiswell, R.: The low-temperature geochemical cycle of iron: from continental fluxes to marine sediment deposition, Am. J. Sci., 302, 774–805, 2002.

BGD
9, 8475–8539, 2012

Rabouille, C., Mackenzie, F. T., and Ver, L. M.: Influence of the human perturbation on carbon, nitrogen: and oxygen biogeochemical cycles in the global coastal ocean, Geochim. Cosmochim. Ac., 65, 3615–3641, 2001.
Raiswell, R.: Towards a global highly reactive iron cycle, J. Geochem. Explor., 88, 436–439, 2006.
Regnier, P., Mouchet, A., Wollast, R., and Ronday, F.: A discussion of methods for estimating residual fluxes in strong tidal estuaries, Cont. Shelf Res., 18, 1543–1571, 1998.
Regnier, P., O'Kane, J. P., Steefel, C. I., and Vanderborght, J. P.: Modeling complex multicomponent reactive-transport systems: towards a simulation environment based on the concept of a knowledge base, Appl. Math. Model., 26, 913–927, 2002.
Reimers, C., Friedrichs, C., Bebout, B., Howd, P., Huettel, M., Jahnke, R., MacCready, P., Ruttenberg, K., Sanford, L., and Trowbridge, J.: Coastal Benthic Exchange Dynamics, Skidaway Institute of Oceanography Technical Report TR-04–01, 92, Savannah, GA, USA, 2004.
Ridgwell, A.: Interpreting transient carbonate compensation depth changes by marine sediment core modeling, Paleoceanography, 22, PA4102, 2007.
Ridgwell, A. and Hargreaves, J. C.: Regulation of atmospheric CO_2 by deep-sea sediments in an Earth system model, Global Biogeochem. Cy., 234, 299–315, 2007.
Rojas, N. and Silva, N.: Early diagenesis and vertical distribution of organic carbon and total nitrogen in recent sediments from southern Chilean fjords (Boca del Guafo to Pulluche Channel), Invest. Mar., 33, 183–194, 2005.
Rusch, A., Huettel, M., Wild, C., and Reimers, C. E., Benthic oxygen consumption and organic matter turnover in organic-poor: permeable shelf sands, Aquat. Geochem., 12, 1–19, 2006.
Sarmiento, J. L. and Gruber, N.: Ocean biogeochemical dynamics, Cambridge University Press, Cambridge, 2006.
Sarmiento, J. L., Hughes, T. M. C., Stouffer, R. J., and Manabe, S.: Simulated response of the ocean carbon cycle to anthropogenic climate warming, Nature, 393, 245–249, 1998.
Schneider, R. R., Schulz, H. D., and Hensen, C.: Marine carbonates: their formation and destruction, Mar. Geochem., 311–337, 2006.
Shaffer, G., Malskær Olsen, S., and Pepke Pedersen, J. O.: Presentation, calibration and validation of the low-order, DCESS Earth System Model (Version 1), Geosci. Model Dev., 1, 17–51, doi:10.5194/gmd-1-17-2008, 2008.
Smith, W. H. F. and Sandwell, D. T.: Global sea floor topography from satellite altimetry and ship depth soundings, Science, 277, 1956, 1997.

BGD
9, 8475–8539, 2012

Soetaert, K., Middelburg, J. J., Wijsman, J., Herman, P., and Heip, C.: Ocean margin early diagenetic processes and models, in: Ocean Margin Systems, Springer, Berlin, 157–177, 2002.
Spiteri, C., Van Cappellen, P., and Regnier, P.: Surface complexation modeling of phosphate adsorption to iron(III)(hydr)oxides along pH and salinity gradients in estuaries and coastal aquifers, Geochim. Cosmochim. Ac., 72, 3431–3445, 2008.
Stockman, K. W., Ginsburg, R. N., and Shinn, E. A.: The production of lime mud by algae in South Florida, J. Sediment Petrol., 37, 633–648, 1967.
Suchet, A., Probst, J. L., and Ludwig, W.: Worldwide distribution of continental rock lithology: Implications for the atmospheric/soil CO_2 uptake by continental weathering and alkalinity river transport to the oceans, Global Biogeochem. Cy., 17, 1038–1051, 2003.
Takahashi, T., Broecker, W. S., and Bainbridge, A. E.: The alkalinity and total carbon dioxide concentration in the world oceans, in: Carbon Cycle Modelling, John Wiley and Sons, New York, 159–200, 1981.
Thomas, H., Schiettecatte, L., Suykens, K., Koné, Y. J. M., Shadwick, E. H., Prowe, A. E. F., Bozec, Y., de Baar, H. J. W., and Borges, A. V.: Enhanced ocean carbon storage from anaerobic alkalinity generation in coastal sediments, Biogeosciences, 6, 267–274, 2009, http://www.biogeosciences.net/6/267/2009/.
Thullner, M., van Cappellen, P., and Regnier, P.: Modeling the impact of microbial activity on redox dynamics in porous media, Geochim. Cosmochim. Ac., 69, 5005–5019, 2005.
Thullner, M., Dale, A. W., and Regnier, P.: Global-scale quantification of mineralization pathways in marine sediments: a reaction-transport modeling approach, Geochem. Geophys. Geosy., 10, Q10012, 2009.
Turner, R. E. and Rabalais, N. N.: Linking landscape and water quality in the Mississippi River Basin for 200 years, BioScience, 53, 563–572, 2003.
Walter, L. M. and Morse, J. W.: The dissolution kinetics of shallow marine carbonates in seawater: a laboratory study, Geochim. Cosmochim. Ac., 49, 1503–1513, 1985.
Wang, Y. and Van Cappellen, P.: A multicomponent reactive transport model of early diagenesis: application to redox cycling in coastal marine sediments, Geochim. Cosmochim. Ac., 60, 2993–3014, 1996.
Westrich, J. T. and Berner, R. A.: The role of sedimentary organic matter in bacterial sulfate reduction: the G model tested, Limnol. Oceanogr., 236–249, 1984.

BGD
9, 8475–8539, 2012

Wollast, R.: The coastal organic carbon cycle: fluxes, sources and sinks, in: Ocean Margin Processes in Global Change, Wiley, London, 365–381, 1991.
Wollast, R. and Mackenzie, F. T.: Global biogeochemical cycles and climate, NATO ASI Ser. C Math. Phys. Sci., 285, 453–473, 1989.

BGD
9, 8475–8539, 2012

Table 1. Global C flux estimates in coastal sediments.

	Global estimate (Tmol C yr^{-1})	Reference
POC deposition flux	16	Jahnke (2010)
	19	Jahnke (1996)
	40 (pre-industrial)	Andersson et al. (2005)
	52	Muller-Karger et al. (2005)
	97 (0–150 m, reactive only)	Thullner et al. (2009)
	135	Dunne et al. (2007)
	140	This work
	167	Wollast (1991)
	183	Sarmiento and Gruber (2006)
POC burial	11 (shelf deltaic muds)	Berner (1982)
	15	Chen (2002)
	14.5	Sarmiento and Gruber (2006)
	17	Wollast (1991)
	18–20	Wollast and Mackenzie (1989)
	20	Mackenzie et al. (1998)
	22 (inert POC not explicitly modeled)	This work
	60	Dunne et al. (2007)
PIC deposition	23	Milliman and Droxler (1996)
	23	This work
	24.5 (not including inert riverine PIC)	Andersson et al. (2005)
PIC burial	13	Milliman and Droxler (1996)
	14.5 (not including inert riverine PIC)	Andersson et al. (2005)
	15	Chen (2002)
	16	This work
	17	Feely et al. (2004)
	21	Mackenzie et al. (1998)

BGD
9, 8475–8539, 2012

Table 2. Hierarchical classification scheme (see text for details).

	Controlling factor	Characteristics	Scenarios
Level I	Mode of carbonate production/accumulation	J_{PIC}	1 Reefs, 2 Banks and embayments, 3 Carbonate shelves, 4 Non-carbonate shelves
Level II	Carbonate dissolution	J_{POC}, O_2, NO_3, SO_4	1 Globally average conditions for reefs 2 Globally average conditions for banks and embayments 3 Globally average conditions for carbonate shelves 4 Globally average conditions for noncarbonate shelves
Level III	Local variability	Water depth master variable for variability in J_{POC}, J_{PIC}, O_2, NO_3, SO_4, w, α, D_b	1 Average water depth 25 m 2 Average water depth 25 m 3 25, 75, 150 m 4 25, 75, 150 m

BGD
9, 8475–8539, 2012

Table 3. Kinetic and equilibrium reactions, and generation of DIC and A_T.

	Reaction	DIC	A_T
	Hydrolysis		
R1, R2	$\frac{1}{106}(CH_2O)_{106}(NH_3)_{16}(H_3PO_4) + \frac{15}{106}H^+ \rightarrow CH_2O + \frac{16}{106}NH_4^+ + \frac{1}{106}H_2PO_4^-$	0	+0.14
	Primary redox reactions		
R3	$CH_2O + O_2 \rightarrow CO_2 + H_2O$	+1	0
R4	$CH_2O + 0.8NO_3^- + 0.8H^+ \rightarrow CO_2 + 0.4N_2 + 1.4H_2O$	+1	+0.8
R5	$CH_2O + 4Fe(OH)_3 + 8H^+ \rightarrow CO_2 + 4Fe^{2+} + 11H_2O$	+1	+8
R6	$CH_2O + 1/2\ SO_4^{2-} + 1/2\ H^+ \rightarrow CO_2 + 1/2\ HS^- + H_2O$	+1	+1
	Secondary redox reactions		
R7	$1/2\ NH_4^+ + O_2 \rightarrow 1/2\ NO_3^- + 1/2\ H_2O + H^+$	0	−1
R8	$4Fe^{2+} + O_2 \rightarrow 4Fe(OH)_3 + 8H^+$	0	−8
R9	$1/2\ HS^- + O_2 \rightarrow 1/2\ SO_4^- + 1/2\ H^+$	0	−1
R10	$1/2\ FeS + O_2 \rightarrow 1/2\ Fe^{2+} + 1/2\ SO_4^{2-}$	0	0
	PIC dissolution		
R11	$CaCO_3(calcite) \rightarrow Ca^{2+} + CO_3^{2-}$	+1	+2
R12	$CaCO_3(aragonite) \rightarrow Ca^{2+} + CO_3^{2-}$	+1	+2
R13	$Ca_{0.85}Mg_{0.15}CO_3 \rightarrow 0.85Ca^{2+} + 0.15Mg^{2+} + CO_3^{2-}$	+1	+2
	Other kinetic reactions		
R14	$Fe^{2+} + HS^- \rightarrow FeS + H^+$	0	−2
R15	$FeS + H_2S \rightarrow H_2 + FeS_2$	0	0
R16	$Fe^{2+} + CO_3^{2-} \rightarrow FeCO_3$	−1	−2
R17	H_2S + inert-POC → organic-S	0	0
	Equilibria		
	$H_2CO_3^* \leftrightarrow H^+ + HCO_3^-$		
	$HCO_3^- \leftrightarrow H^+ + CO_3^{2-}$		
	$H_2O \leftrightarrow H^+ + OH^-$		
	$H_2S \leftrightarrow H^+ + HS^-$		
	$B(OH)_3 + H_2O \leftrightarrow H^+ + B(OH)_4^-$		
	$Fe(OH)_3 + H_2PO_4^- \leftrightarrow$ iron-sorbed-P		
	$H_2PO_4^- \leftrightarrow$ sorbed-P		
	$Fe^{2+} \leftrightarrow$ sorbed-Fe		
	$NH_4^+ \leftrightarrow$ sorbed-NH_4		

Reaction numbers for reference to Tables 2 and 3.
DIC – mol of DIC generated or consumed for the reaction as written.
A_T – eq. of alkalinity generated or consumed for the reaction as written.
Equilibrium reactions do not lead to any net generation of DIC or alkalinity.

BGD
9, 8475–8539, 2012

Table 4. Kinetic rate laws.

Reaction	
$R1 = k_{POC1} \cdot [POC1]$	
$R2 = k_{POC2} \cdot [POC2]$	
$R3 = k_3 \cdot \left(\frac{[O_2]}{k_{O_2} + [O_2]}\right) \cdot [CH_2O]$	
$R4 = k_3 \cdot \left(\frac{Y_{NO_3}}{Y_{O_2}}\right) \cdot \left(\frac{[NO_3]}{k_{NO_3} + [NO_3]}\right) \cdot [CH_2O] \cdot \left(\frac{ki_{NO_3}}{ki_{NO_3} + [O_2]}\right)$	
$R5 = k_3 \cdot \left(\frac{Y_{Fe}}{Y_{O_2}}\right) \cdot \left(\frac{[Fe(OH)_3]}{k_{Fe} + [Fe(OH)_3]}\right) \cdot [CH_2O] \cdot \left(\frac{ki_{Fe}}{ki_{Fe} + [O_2]}\right)$	
$R6 = k_3 \cdot \left(\frac{Y_{SO_4}}{Y_{O_4}}\right) \cdot \left(\frac{[SO_4]}{k_{SO_4} + [SO_4]}\right) \cdot [CH_2O] \cdot \left(\frac{ki_{SO_4}}{ki_{SO_4} + [O_2]}\right)$	
$R7 = k_{Nitrif} \cdot [NH_4^+] \cdot [O_2]$	
$R8 = k_{FeO_x} \cdot [O_2] \cdot [Fe^{2+}]/[H^+]^2$	
$R9 = k_{SulfO_x} \cdot [O_2] \cdot ([HS^-] + [H_2S])$	
$R10 = k_{FeSO_x} \cdot [FeS] \cdot [O_2]$	
$R11 = k_{Cal}(1-\Omega_{Cal})^{n\text{Cal}}$	$\Omega_{Cal} < 1$
$R12 = k_{Ara}(1-\Omega_{Ara})^{n\text{Ara}}$	$\Omega_{Ara} < 1$
$R13 = k_{Mg\text{-}cal}(1-\Omega_{Mg\text{-}cal})^{n\text{Mg-cal}}$	$\Omega_{Mg\text{-}cal} < 1$
$R14 = k_{FeS} \cdot \left(\frac{[Fe^{2+}] \cdot [HS^-]}{[H^+] \cdot Ks_{FeS}} - 1\right)$	$R14 \geq 0$
$R15 = k_{Pyr} \cdot [FeS] \cdot [H_2S]$	
$R16 = k_{FeCO_3} \cdot \left(\frac{[Fe^{2+}] \cdot [CO_3^{2-}]}{Ks_{FeCO_3}} - 1\right)$	$R16 \geq 0$
$R17 = k_{OrgS} \cdot [\text{inert-POC}] \cdot [H_2S]$	

BGD
9, 8475–8539, 2012

Table 5. Selected parameters for kinetic equations.

Parameter	Value	Units	Note
k_{POC1}	1	yr^{-1}	
k_{POC2}	0.1	yr^{-1}	
k_{POC3}	0	yr^{-1}	
k_{O_2}	20	μM	a
k_{NO_3}	5	μM	a
k_{Fe}	1	$\mu mol\, g^{-1}$	a
k_{SO_4}	1600	μM	a
Y_{NO_3}/Y_{O_2}	0.75	–	a
Y_{Fe}/Y_{O_2}	0.25	–	a
Y_{SO_4}/Y_{O_2}	0.2	–	a
ki_{NO_3}	7	μM of O_2	b
ki_{Fe}	0.7	μM of O_2	b
ki_{SO_4}	0.7	μM of O_2	b
k_{Nitrif}	10000	$mM^{-1}\, yr^{-1}$	c
k_{FeO_x}	3.6×10^{-6}	$mM\, yr^{-1}$	d
k_{SulfO_x}	320–320 000	$mM^{-1}\, yr^{-1}$	e
k_{Cal}	40	$mM^{-1}\, yr^{-1}$	f
n_{Cal}	2.74	–	f
k_{Ara}	110	$mM^{-1}\, yr^{-1}$	f
n_{Ara}	2.43	–	f
$k_{Mg\text{-}cal}$	58	$mM^{-1}\, yr^{-1}$	f
$n_{Mg\text{-}cal}$	3.61	–	f
k_{FeS}	0.005	$\mu mol\, cm^{-3}\, yr^{-1}$	c
Ks_{FeS}	6.3	$\mu mol\, cm^{-3}$	c
k_{Pyr}	60	$cm^3\, \mu mol^{-1}\, yr^{-1}$	g
k_{OrgS}	0.0002	$cm^3\, \mu mol^{-1}\, yr^{-1}$	g

[a] Thullner et al. (2005).
[b] Wang and van Cappellen (1996).
[c] Jourabchi et al. (2005).
[d] Adjusted for T and seawater from Stumm and Morgan (1995).
[e] See Sect. 2.6.1.
[f] Recalculated from Walter and Morse (1985).
[g] Dale et al. (2009).

BGD
9, 8475–8539, 2012

Table 6a. Boundary conditions, baseline case.

Parameter		Environment "Carbonate" shelf	"Non-carbonate" shelf	Banks and bays	Reefs
Fluxes (mol m^{-2} $^{-1}$)					
POC	25 m	6.46	6.46	6.46	5.20
	75 m	3.45	3.45		
	150 m	2.32	2.32		
$Fe(OH)_3$	25 m	0.038	0.038	0.038	0.038
	75 m	0.036	0.036		
	150 m	0.033	0.033		
Calcite		0.39	0.17	0.65	1.95
Aragonite		0.21	0.09	3.15	9.45
15 % Mg-calcite		0	0	1.20	3.60
Concentrations (mM)					
O_2		0.195	0.195	0.195	0.195
NO_3^{-} [a]	25 m	0.005	0.005	0.005	0.005
	75 m	0.008	0.008		
	150 m	0.012	0.012		
SO_4^{2-}		28	28	28	28
$H_2PO_4^{-}$		0.001	0.001	0.001	0.001
Ca^{2+}		10	10	10	10
A_T		2.306	2.306	2.306	2.306
DIC[a]	25 m	2.022	2.022	2.022	2.022
	75 m	2.068	2.068		
	150 m	2.138	2.138		
CO_3^{2-}	25 m	0.201	0.201	0.201	0.215
	75 m	0.170	0.170		
	150 m	0.124	0.124		
Temperature (°C)	25 m	14.34	14.34	9.91	27.6
	75 m	11.63	11.63		
	150 m	7.57	7.57		
pH (free scale)	25 m	8.27	8.27	8.27	7.95
	75 m	8.19	8.19		
	150 m	8.04	8.04		
$\Omega_{Aragonite}$ [b]	25 m	2.98	2.98	2.98	3.19
	75 m	2.55	2.55		
	150 m	2.01	2.01		

[a] Nitrate and DIC concentrations determined from SFD correlations found in GLODAP database:

$[NO_3]$ (mM) = $0.003734 + 0.0000584 \cdot SFD$ $\quad (r^2 = 0.250, p < 10^{-195})$

[DIC] (mM) = $1.9992 + 0.0009220 \cdot SFD$ $\quad (r^2 = 0.262, p < 10^{-5})$

[b] $\Omega_{Aragonite}$ calculated from Millero (1995) using pressure, salinity, and the following temperature correlation extracted from the Levitus94 database:

Temp (°C) = $15.69 - 0.054 \cdot SFD$ $\quad (r^2 = 0.098, p < 10^{-42})$

BGD
9, 8475–8539, 2012

Table 6b. Boundary pH and $\Omega_{Aragonite}$ for DIC sensitivity tests.

Parameter		Environment "Carbonate" shelf	"Non-carbonate" shelf	Banks and bays	Reefs
+2.5 % DIC					
pH	25 m	8.18	8.18	8.18	7.86
	75 m	8.08	8.08		
	150 m	7.90	7.90		
$\Omega_{Aragonite}$	25 m	2.55	2.55	2.55	2.85
	75 m	2.10	2.10		
	150 m	1.47	1.47		
+5 % DIC					
pH	25 m	8.07	8.07	8.07	7.76
	75 m	7.95	7.95		
	150 m	7.74	7.74		
$\Omega_{Aragonite}$ [a]	25 m	2.07	2.07	2.07	2.34
	75 m	1.63	1.63		
	150 m	1.05	1.05		

BGD
9, 8475–8539, 2012

Table 7. Benthic C and alkalinity fluxes by environment, baseline case.

	Reefs	Banks and bays	"Carbonate" shelves	"Non-carbonate" shelves	Total
Area[a] 10^{12} m^2	0.6	0.8	10	15	26.4
PIC in[a] Tmol yr^{-1}	9	4	6	4	23
POC in[b] Tmol yr^{-1}	3.1	5.2	43.7	65.6	117
Model outputs					
Aerobic C oxidation Tmol yr^{-1}	0.5	0.6	6.1	9.2	16.4
Denitrification Tmol yr^{-1}	0.1	0.1	1.2	1.8	3.2
Fe reduction Tmol yr^{-1}	0.01	0.02	0.20	0.29	0.51
Sulfate reduction Tmol yr^{-1}	2.5	4.4	36.1	54.1	97.3
PIC dissolution Tmol yr^{-1}	0.4	0.6	2.7	3.1	6.8
Sediment PIC %	91	28	2.8	1.1	–
DIC out Tmol yr^{-1}	3.5	5.9	47.0	69.4	126
A_T out Teq yr^{-1}	3.7	6.4	47.7	69.5	127
A_T^* Teq yr^{-1}	1.1	1.9	11.1	14.6	29

[a] Milliman and Droxler (1996).
[b] Hatcher (1990) for reefs; the rest from depth-dependency of Soetaert et al. (2002).

BGD
9, 8475–8539, 2012

Table 8. Global estimated benthic fluxes and PIC burial efficiency; POC, DIC and PIC sensitivity.

Reactive POC flux Tmol yr^{-1}	SO_4^{2-} red. (%)	DIC out Tmol yr^{-1}	Pyrite Tmol yr^{-1}	A_T Teq yr^{-1}	A_T^* Teq yr^{-1}	PIC burial efficiency (%) Calcite	Ara.	Mg-cal.
15	45	15	0.34	7	3	100	100	100
29	62	31	0.46	22	6	100	94	97
59	75	64	0.35	58	15	97	73	87
118	83	126	0.32	127	29	72	70	70
176	86	186	0.32	195	41	57	68	65
118[a]	83	127	0.29	130	31	59	69	67
118[b]	83	128	0.27	132	33	48	68	64
118[c]	83	124	0.31	123	24	40	65	51

[a] Bottom water DIC increased by 2.5 %.
[b] Bottom water DIC increased by 5 %.
[c] PIC deposition decreased by 56 %.

BGD
9, 8475–8539, 2012

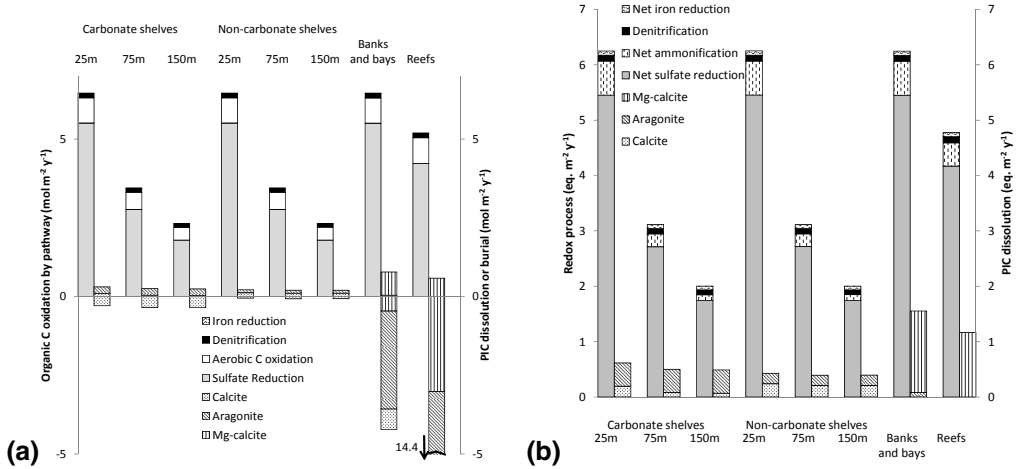

Fig. 1. Processes generating DIC **(a)** and alkalinity **(b)** for the banks and bays, reef, carbonate shelf, and non-carbonate shelf environments. Baseline POC flux. Processes contributing <1 % to the total are not shown.

BGD
9, 8475–8539, 2012

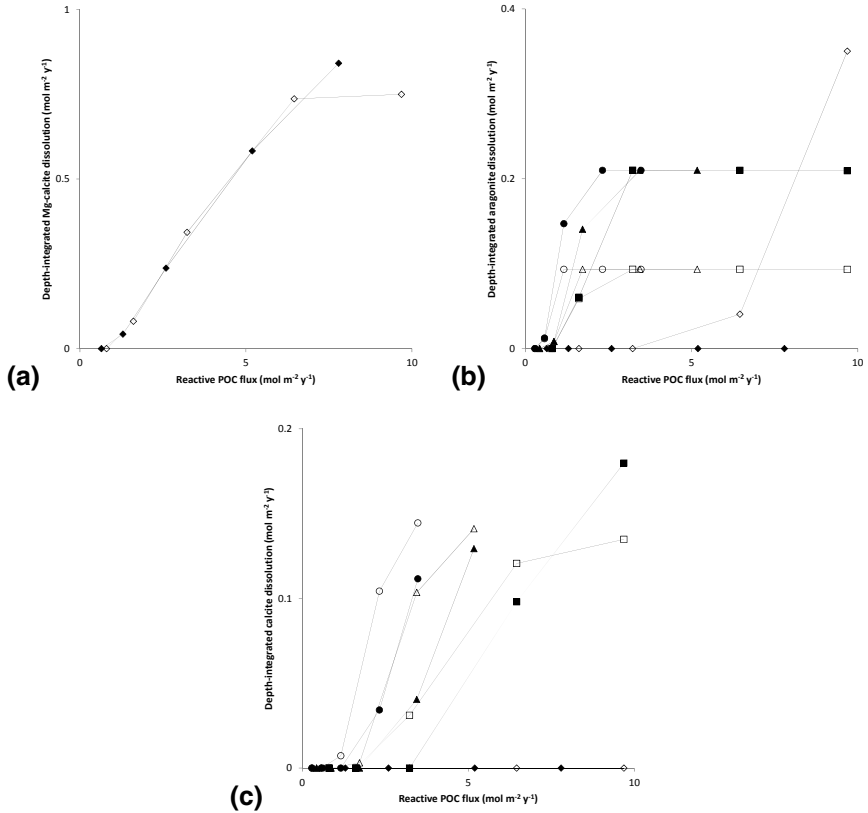

Fig. 2. Depth-integrated dissolution of **(a)** 15 % Mg-calcite, **(b)** aragonite, and **(c)** calcite. Banks and bays (◊), reefs (♦), carbonate shelves: 25 m (■), 75 m (▲), and 150 m (●); non-carbonate shelves: 25 m (□), 75 m (△), and 150 m (○). 15 % Mg-calcite present only in reefs and banks and bays.

BGD
9, 8475–8539, 2012

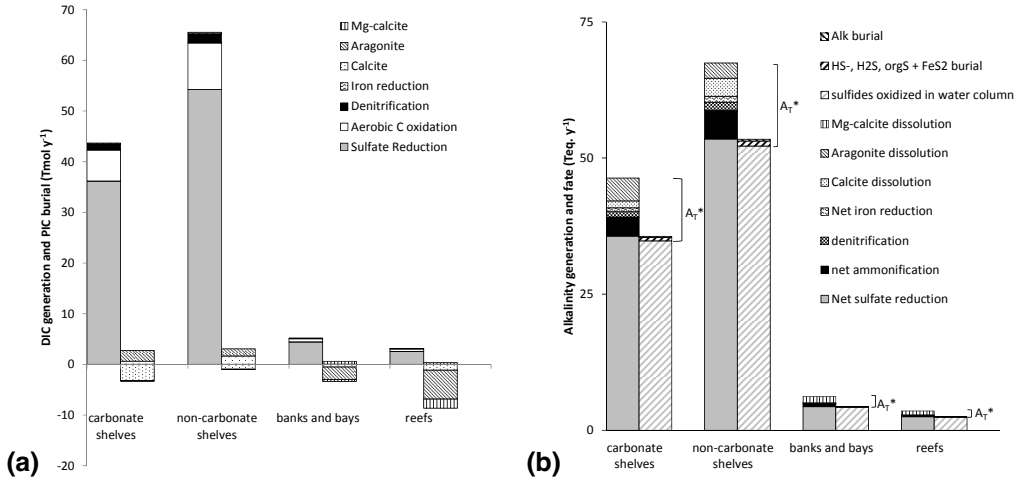

Fig. 3. Generation of DIC **(a)** and Alkalinity **(b)**, along with the fate of generated Alkalinity and PIC by environment. Baseline coastal benthic POC deposition fluxes. **(a)** First column is DIC generation by C oxidation pathway, second column is PIC dissolution or burial. **(b)** First column is Alkalinity generation by redox reactions and PIC dissolution, second column is the fate of the liberated alkalinity (burial, release to the water column as A_T^*, release to the water column as sulfides).

BGD
9, 8475–8539, 2012

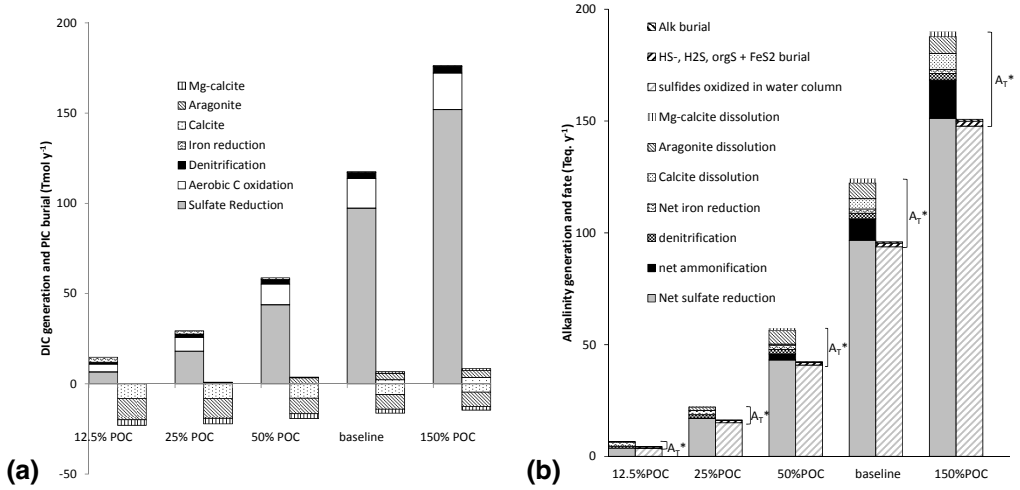

Fig. 4. Global generation of DIC **(a)** and Alkalinity **(b)**, along with the fate of generated Alkalinity and PIC. Baseline coastal benthic POC deposition fluxes. **(a)** First column is DIC generation by C oxidation pathway, second column is PIC dissolution or burial. **(b)** First column is Alkalinity generation by redox reactions and PIC dissolution, second column is the fate of the liberated alkalinity (burial, release to the water column as A_T^*, release to the water column as sulfides).

BGD
9, 8475–8539, 2012

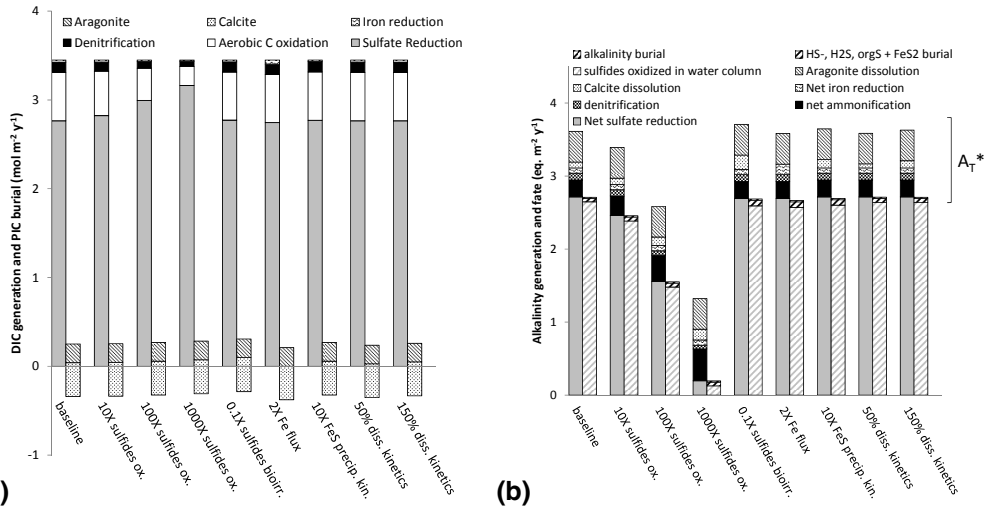

Fig. 5. Model output DIC **(a)** and alkalinity **(b)** generation sensitivity to dissolution kinetics, sulfide bioirrigation, sulfide oxidation kinetics, Fe deposition, and FeS precipitation kinetics. 75 m "carbonate shelf" environment.

BGD
9, 8475–8539, 2012

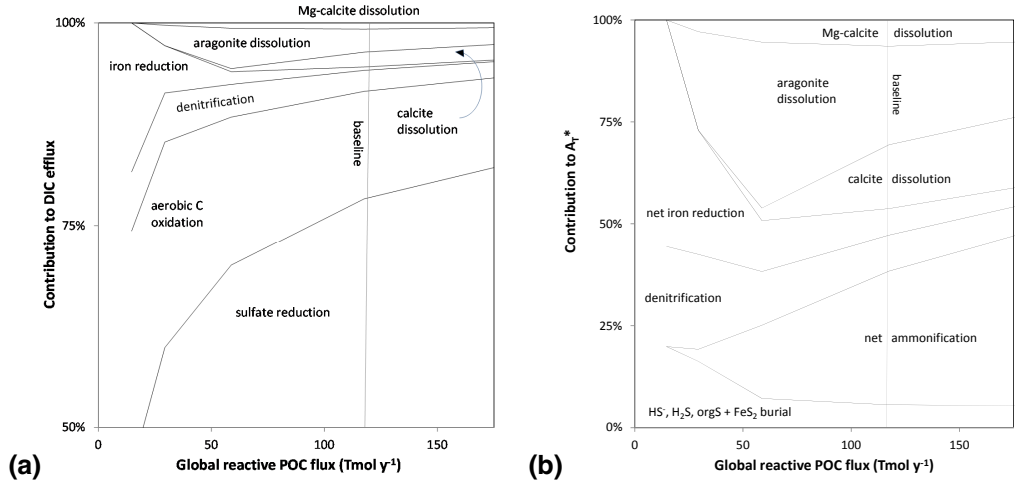

Fig. 6. Contributions of individual redox processes and PIC dissolution to DIC efflux **(a)** and A_T^* **(b)** vs. POC deposition flux.

BGD
9, 8475–8539, 2012

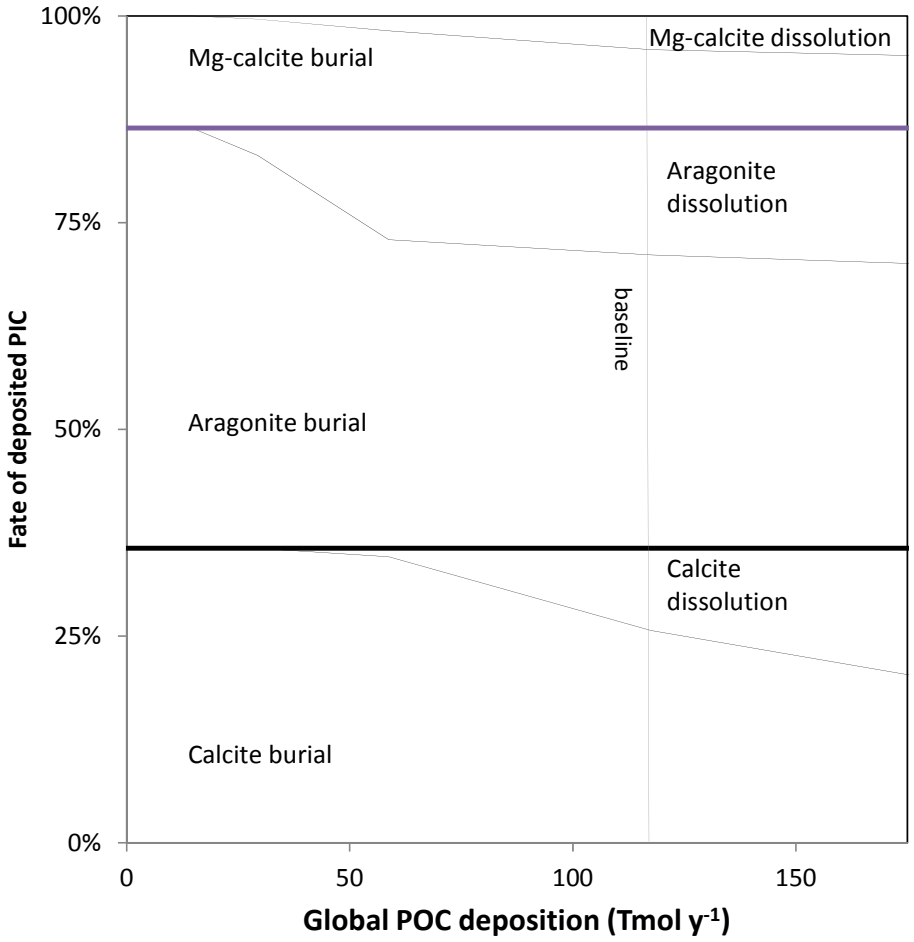

Fig. 7. Fate of PIC. Global dissolution or burial of $CaCO_3$ phases as a function of POC deposition.

BGD
9, 8475–8539, 2012

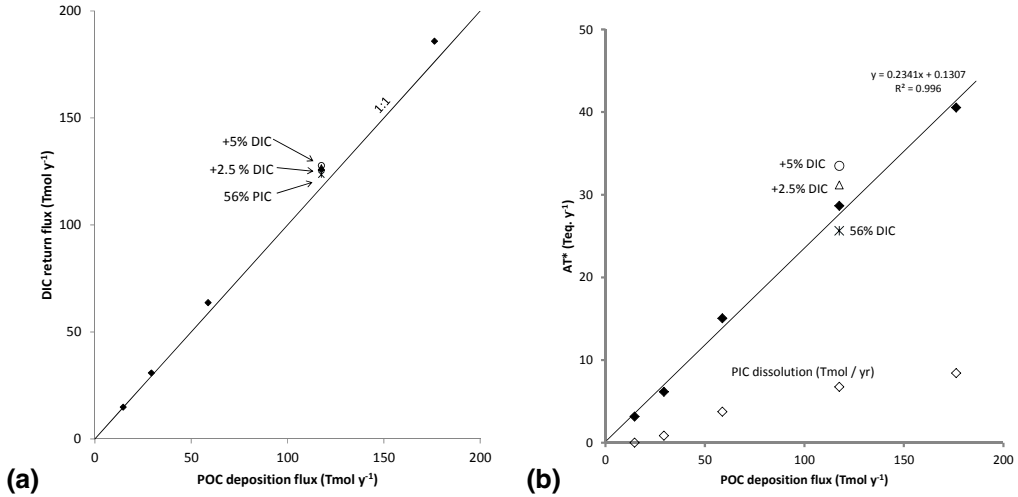

Fig. 8. Global coastal DIC return flux **(a)**, A_T^* **(b)**, and PIC dissolution **(b)**, vs. POC deposition flux.

BGD
9, 8475–8539, 2012